Universitat Rovira i Virgili

Escola Tècnica Superior d'Enginyeria Química

Universidad Internacional de La Rioja

Escuela Superior de Ingeniería y tecnología

Máster Interuniversitario en Mecánica de Fluidos Computacional

Evaluation of wind concentrator in a single-row wind farm.

Trabajo fin de estudio presentado por:	María Manuela Rosales Cardenal
Tipo de trabajo:	Trabajo final de máster.
Director/a:	Antonio Vernet Peña
Fecha:	Junio 2024

Acknowledgments

I'd like to dedicate this work to my family and thank them for their support and patience in the journey that has been the present Master.
I'd like to thank my supervisor for his patience and guidance to build this work.
I'd like to thank W'WAVE for allowing me to develop the project which has opened for me the road to new knowledge and the building of new skills.
Big thanks to all the researchers who kindly replied to my communications and shared knowledge with a stranger: Martin Paul van der Laan, Matías Ávila, Mihael Cindori, Gonzalo Navarro and Saugat Shrestha. It's admirable their sense of solidarity.
Finally but not last, thank God for allowing me to start and close this journey.

Abstract

Here is presented an evaluation in CFD steady-state RANS of the use of a concentrator in a real case of a single-row modeled wind farm in flat terrain to optimize the wind energy production of the concentrated system. The target wind farm was the Shagaya Renewable Park in Kuwait which consists of 5 units of wind turbines Siemens Gamesa G97/2MW of diameter and hub of 97 and 80 m, which were modeled by the actuator disk model approach. For treating the wake-affected conditions of the turbines due to the presence of a concentrator, four different implementations for computing the thrust were tested: CC, NC, CA and CF. The concentrated system was set on the first three wind turbines, which were covered with a nonporous concentrator of 810 m length and of 12 m height, h, at three upwind distances x_t/h: 2, 4, and 7; which the optimal was to be determined. Since the unavailability of large-scale field measurements of a concentrator performing with an operative wind turbine, the present model validation relies on the quality of the validation by similarity cases performed separated for atmospheric flow over buildings and actuator disk modeling.

The results illustrated different predictions of the increment of wind power production for the four implementations. As for the CC and NC implementations, by slight difference from 4h distance, 2h distance provided the highest increment in power production in the concentrated system of 18.49% and tendency of decay of this benefit as the distance increases. As per the CA approach, the slight difference between 2h and 4h remained but, the highest values at 4h were found to be 17.62%. Last, the CF method showed outstanding performance of increment of 49.0% by placing in this case the assumption of remaining constant the magnitude of the thrust magnitude while having the concentrator.

Keywords: Actuator disk, RANS, Optimized wind, Concentrator, Wind farm.

Contents

Acknowledgments **i**

Abstract **ii**

Introduction **1**

1 Theorethical framework **6**

1.1 ABL modeling 6

1.1.1 Turbulence model 7

1.1.2 Boundary conditions 10

1.1.3 Walls and y+ 12

1.2 Actuator disk modeling 13

1.2.1 ADM approaches 15

1.2.2 Load distribution in disk 16

1.2.3 Wake-affected turbines 17

1.3 Windbreaks 19

1.3.1 Windbreak models on windfarms 19

1.3.2 Literature limitations 21

2 Methodology **22**

2.1 Project description 22

2.1.1 W'wave 22

2.1.2 Shagaya Wind Project 22

2.1.3 W'wave's proposal 23

2.2 Objectives 24

2.2.1 Specific objectives 24

2.3 General numerical setup . . . 24
2.4 Validation case of ABL flow over building . . . 25
2.4.1 Domain and mesh . . . 25
2.4.2 Boundary conditions . . . 26
2.4.3 Numerical schemes . . . 27
2.4.4 Mesh convergence . . . 27
2.4.5 Results of validation . . . 29
2.5 Validation case of ADM . . . 30
2.5.1 Domain and background mesh . . . 30
2.5.2 Boundary conditions . . . 31
2.5.3 Numerical setup . . . 32
2.5.4 Mesh sensitivity study . . . 32
2.5.5 Results of validation . . . 34
2.5.6 Revision between uniform and nonuniform load . . . 34
2.5.7 Wake affected turbine . . . 35

3 Pre-processing **37**
3.1 Description of the model . . . 37
3.1.1 Concentrator and tested locations . . . 38
3.1.2 G97 turbine data and tested actuator disk submodels . . . 38
3.1.3 Parameters for evaluation . . . 39
3.2 Mesh sensitivity study . . . 39
3.2.1 Mesh convergence study . . . 40
3.2.2 Wall refinement and y+ . . . 42
3.2.3 Tables for cases with calibration . . . 43

4 Results and discussion **45**
4.1 Concentrated turbines . . . 45
4.1.1 Statistical values . . . 45
4.1.2 Overall changes in regions . . . 49
4.2 Net power capacity increase . . . 51
4.2.1 Theoretical solution . . . 51
4.2.2 Comparison between cases . . . 51

4.2.3 Locations and gains 53
4.2.4 Changes in non-concentrated turbines: N4 and N5 53
4.2.5 Overall net power increase in the concentrated wind farm 54
4.3 Signs of a new operative condition 55
4.3.1 Relationship between thrust and net power increase 55
4.3.2 Theoretical approach to the new condition 55

Conclusions **57**
Future work 59

References **61**

A Appendix **69**
A.1 Met-mast analysis of Shagaya 69
A.2 Hybrid inlet profile U for CIEMAT 69
A.3 vectorCodedSource NREL thrust distribution 70
A.4 vectorCodedSource Variable thrust force controller 72

List of Figures

1 Scheme of a generic case of concentrator centered to a turbine. Left: key dimensional variables of the layout, Right: Flow deflection, horizontal wind velocity plotted in contour map. 3

2 Picture of the Shagaya Renewable Park in Kuwait (KSIR, n.d.) 4

2.1 Wind concentrator proposal for Shagaya Wind Project 23

2.2 Domain and mesh preview (mirror view) of CIEMAT validation case. Green box: refinement regions tested. Red box: close-up of the concentrator design from sea-ship containers 26

2.3 Mesh sensitivity convergence. 28

2.4 Close-up of nearby refinement and boundary layer of concentrator. 28

2.5 Wake contours of horizontal wind velocity of $k - \varepsilon - f_P$ solution. Left: Plane at the center of concentrator with iso-lines of several velocity levels. Right: Plane at half the height of the concentrator. 29

2.6 Model validation, experimental measurements from Martí (2020) 30

2.7 Domain dimension and mesh discretization in actuator disk validation. Red marker: cellSet of ADM. 31

2.8 Mesh sensitivity study in horizontal-uniform refinement of the wake of the ADM 32

2.9 Extrapolated solution and error for the first mesh study. 33

2.10 Comparison between normalized load distribution used on NREL case study and theoretical. 34

2.11 Mesh sensitivity study in non-uniformly loaded actuator disk: at downstream distances of x/D: 2.5, 5, and 7.5. 34

2.12 Comparison of wakes between models in horizontal velocity wake deficit (top), and turbulent intensity (bottom). 35

2.13 Comparison between models of constant thrust force magnitude and variable thrust. 36

3.1 Overall top view of the inside of the mesh. Red line: concentrator. Green circles: concentrated sub-system. Black circles: rotors N4 and N5. 40

3.2 A cut-plane view centered at concentrator half of meshes Fine (left), medium (center) and coarse (right). 41

3.3 Comparison between solutions of only wind turbines models vs. the presence of concentrator using the 'fine mesh. (a-c) Only WT in wind farm, (d-f) wind farm with concentrator. 43

3.4 Local refinement at concentrator walls (left) and y+ contour map at an extreme side, windward face view (right). 44

4.1 Speed-up of horizontal wind velocity (top) and changes in TI (bottom) at hub point. 46

4.2 Speed-up of horizontal wind velocity (top) and changes in TI (bottom) at disk-average. 47

4.3 Comparison of vertical profiles of horizontal wind velocity before and after the presence of concentrator taken at rotor plane of turbine N2. 48

4.4 Contour of wind speed changes in the close area of wind turbine N2 by each ADM method with a 4h distance. Dashed lines delimit the rotor region. Solid line: rotor's location. Dashed lines: lower and upper tips of the rotor. 50

4.5 Contour of turbulence intensity changes in the close area of wind turbine N2 by each ADM method with a 4h distance. Dashed lines delimit the rotor region.Solid line: rotor's location. Dashed lines: lower and upper tips of the rotor. 50

4.6 Contour of changes in wind velocity and turbulence intensity changes at the rotor plane of rotors for case CC at 4h distance. Cross markers: wind turbine hub points. Dashed lines: lower and upper tips of the rotor. 51

4.7 Ratio of wind power increase of the concentrated wind turbines system if computed from hub values (left) and if computed from disk-average values (right). 52

4.8 Weighted solution of wind power increase based on hub and disk-average values. 53
4.9 Wind power increase in non-concentrated turbines: N4 and N5. 54
4.10 Overall wind power increase in Shagaya's wind farm. 55
4.11 Comparison of wind power increase at hub point of N2 against changes in the thrust magnitude between solutions with and without concentrator. . . 56

A.1 Weibull distribution of wind speed 69
A.2 Wind speed rose 69

List of Tables

1.1 Constants for $k-\varepsilon$ turbulence model 8
1.2 Constants for $k-\varepsilon-f_P$ turbulence model 9

2.1 Description of meshes 26
2.2 Y^+ mesh characteristics 29
2.3 $\kappa-\varepsilon$ and $\kappa-\varepsilon-f_P$ comparison at rotor region 30
2.4 Input parameters for numerical computations 30
2.5 $k-\varepsilon-f_P$ statistics 36
2.6 Comparison of uniform and non-uniform cases 36

3.1 Description of implementation cases of actuator disk 38
3.2 Mesh options summary 40
3.3 Mesh options and levels of refinement applied 41
3.4 Detailed Mesh Data and Convergence Information 42
3.5 Summary of y+ values at wall in fine mesh 42
3.6 Single-turbine runs of G97 for different wind speeds and different load distributions. 44

4.1 Average values gathered from comparison of vertical profiles 49
4.2 Relative error between $\frac{\Delta P}{P_0}$ and theoretical solution. 52

Nomenclature

α	Induction factor [-]
α_c, β	Fitting constants of linear theory [-]
β	Constant [-]
ΔP	Net power capacity increase [W]
Δu	net velocity increase [m/s]
κ	Von Kármán constant [-]
μ	Dynamic viscosity [kg/m·s]
μ_t	Eddy viscosity [kg/m·s]
ν	Kinematic viscosity of the fluid [m^2/s]
ρ	Density [kg/m^3]
σ	dimensionless local shear in $k-\varepsilon-f_P$ model [-]
σ_ε	the turbulence dissipation Prandtl's number [-]
σ_k	the turbulence kinetic energy Prandtl's number [-]
τ_w	Wall shear stress [N/m^2]
ε	dissipation rate of k [m^2/s^3]
$\widetilde{\sigma}$	shear constant in $k-\varepsilon-f_P$ model [-]
A	Swept rotor area [m^2]
b	width of the concentrator [m]

C_μ Viscosity constant [-]

C_P Power coefficient [-]

C_R Calibration constant in $k-\varepsilon-f_P$ model [-]

C_T Thrust coefficient [-]

C'_T Calaf's thrust coefficient [-]

$C_{\varepsilon 2}$, $C_{\varepsilon 1}$ $k-\varepsilon$ turbulence model constants [-]

f_P Function limiter of $k-\varepsilon-f_P$ model [-]

G_k Specific production of turbulent kinectic energy [m^2/s^3]

h height of the concentrator [m]

k turbulent kinetic energy [m^2/s^2]

k_n screen-pressure coefficient [-]

L MOST length scale [m]

l_m Mixing length scale [m]

P Power [W]

P_0 Power capacity without windbreak [W]

P_k Production of k [$kg/m{\cdot}s^3$]

Re Reynolds number[-]

Re_turb Atmospheric turbulent Reynolds number [-]

T Thrust force [N]

$T(z)$ Temperature at a given height z [K]

T_* MOST temperature scale [K]

TI Turbulent intensity [%]

u' Fluctuating wind speed [m/s]

$u(z)$ Wind speed at a given height z [m/s]

U_∞ Undisturbed wind speed velocity at hub height [m/s]

U_d Average in disk wind speed velocity [m/s]

U_N Nominal wind speed of a wind turbine model [m/s]

u_t Wall friction velocity [m/s]

u_* Friction velocity [m/s]

x_t Upwind distance between concentrator and WT [m]

$y+$ Non-dimensional length scale in wall units [-]

z Height above ground [m]

z_{hub} hub-height [m]

z_o Aerodynamic roughness length [m]

Acronyms

ABL Atmospheric Boundary Layer

ADM Actuator Disk Model

ASL Atmospheric Surface Layer

BL Boundary Layer

BR Bloackage Ratio

CFD Computational Fluid Dynamics

$RANS$ Reynolds-Averaged Navier-Stokes

WT Wind Turbine

Introduction

One of the big challenges of recent days is the well-known need to generate electricity with the lowest carbon emissions possible or at least, search for a production system that provides the closest to a zero net balance of this type of emission, to accomplish the century global standards of green energy infrastructure and, to cover the growing demand of powering buildings, transport media, facilities between others modern life needs.

The use of wind flow for the advantage of human civilization is not something new and has been present in history for hundreds of years B.C. from ship transport, water pumping, and grain milling. It was in the 20th century when a new purpose for the wind flow was implemented for electricity generation (EIA, 2023) and since then a new field of research and design called Wind Energy arose and it is still today growing to widen the network of clean and sustainable power electricity production (WindEurope, 2024).

Wind farm installations are a preferable choice in Europe since offer a cost-efficient way of energy production and can coexist within other industrial and urban sectors. Wind farm owners are also taxpayers that benefit the local communities they surround and, due to the large supply chain this technology requires from manufacturing, commissioning, and operation, it is a large worldwide source of employment. Therefore, all these given attributes of the Wind Energy sector assign to this sector an important position in today's world economy (WindEurope, 2024).

In Europe's wind energy sector, it has been registered daily by WindEurope (2024) the wind contribution in the continent's overall electricity generation. In the first quarter of the year 2024, the contribution of the Wind Energy sector to the European overall energy market ranged from 7.7% at its lowest up to 33.8% at its highest. Within these percentages, close to 85% of those values correspond to the onshore wind sector.

The onshore wind sector has been the pioneer in this field of technology. Wind turbines have been placed all over the globe in flat and complex terrains in the arrangement of

single-row or multiple-row wind farms, isolated from or accompanied nearby by other wind farms and urbanism. Final commissioning results from previous campaigns of field measurements and economic analysis of the feasibility of the wind resource of the sites and rate of investment return. Through the years some weaknesses in the Wind Energy sector have arisen in the decision-making process of where to place a wind farm and their layout.

Some scenarios are harmful to wind farm's general efficiency. First, if a new wind farm allocation is set to interfere with the prevailing inflow of an older wind farm and introduces wake to the last one, a decay in the power production of the first wind farm installed will prompt. Second, deficiencies in the measurement campaign study, where prevailing wind directions and annual wind velocities were not properly analyzed led to an overestimation of resources available at a given place. Third, large periods of maintenance, non-availability of turbines or harsh inflow conditions, and last, case-specific financial needs to improve the wind farm's performance and make the farm profitable.

To correct any drop in the efficiency of a wind farm and to cover the growing energy demand, there is a noticeable need to find methods that help to improve the current performance of wind farms. A way that could help this problem is by finding methods that wind turbines produce more energy. Wind turbines are designed for a nominal power capacity that is set to be achieved within a range of wind speeds, where the minimum value of the wind nominal velocity U_N, often places above the annual mean wind speed value $U_{\infty,y}$ of the wind farm's site. At this point, not all times the wind farms are at their 100% capacity, and at worst, on occasions atmospheric flow could even drop close to zero value in velocity conveying a zero temporal production.

What if the inflow can be artificially and intentionally accelerated and led to an increment in power production in the turbines? Does the artificial modification provide a positive impact? Can several methods of modeling the thrust in wind turbines converge in the same solution of artificial modification? Those are the questions linked to a new pioneer technology of modifying intentionally the wind flow to create benefits in power production by considering the presence of a so-called concentrator, which is a structured body placed upfront the turbine and deflecting wind to a new path while accelerating it. The present fig. 1 introduces a generic layout of a concentrator designed for a single wind turbine (rotor swept area represented as a floating disk) where the dimensional variables: b, h,

z_{hub}, x and D, play a key role in the performance of this structure to make possible the flow deviation as it is also shown in the figure.

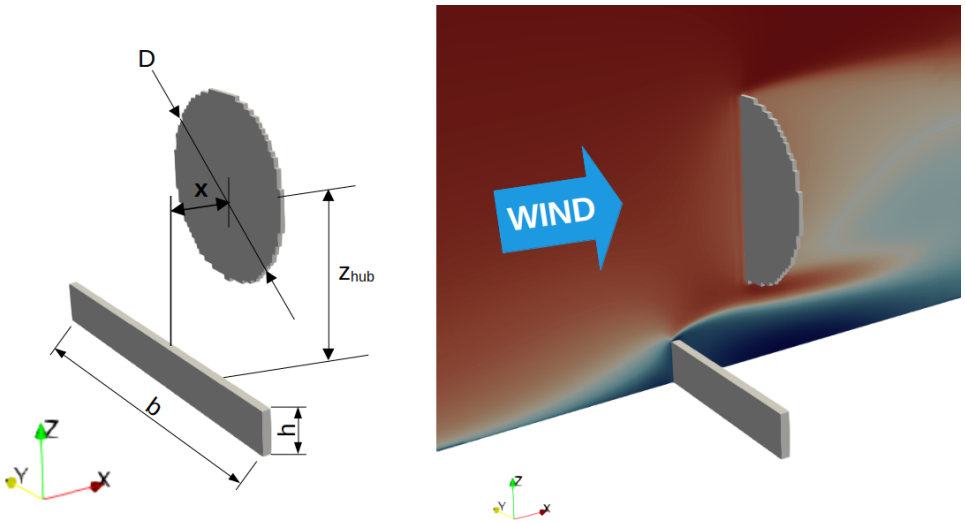

Figure 1: Scheme of a generic case of concentrator centered to a turbine. Left: key dimensional variables of the layout, Right: Flow deflection, horizontal wind velocity plotted in contour map.

Today's state-of-the-art of concentrator integrated already into wind farms is limited to theoretical studies of hypothetical wind turbines, hypothetical site conditions, and hypothetical arrange of windbreaks (Liu & Stevens, 2021; Tobin & Chamorro, 2017; Tobin et al., 2017; Zhang, 2018) and, no real-case field-scale measurements have been documented neither in academia or industry.

A case-specific question arises: will a 'concentrated sub-system' of 3 units from 5 wind turbines G97/2MW, all arranged as a single-row wind farm in Shagaya Renewable Park (Kuwait) benefit from the presence of a long concentrator? This will be the focus topic of the present research, how a long concentrator will perform with a set of turbines of the mentioned wind farm. A picture of the wind farm to be analyzed is presented in fig. 2:

Due to the lack of computational resources and to address a response to the previous inquiry in such a way that any other researcher or industrial Computational Fluid Dynamics (CFD) user could reproduce the present case and, translate this to any other study case, in this research a group of steady-state Reynolds-Averaged Navier-Stokes ($RANS$) CFD simulations were conducted to evaluate the performance of this solid structure already integrated into the modeled wind farm.

New open points to seek answers emerge before approaching a definitive evaluation of the concentrator's performance in power production and hereafter is stated each and how

Figure 2: Picture of the Shagaya Renewable Park in Kuwait (KSIR, n.d.)

were they addressed:

- ◇ The literature of actuator disk modeling mentions several implementations of load distribution and prediction of overall thrust magnitude for wake-affected turbines, does the choice of either of these methods will impact significantly the results? To clarify this, 4 methods will be tested and analyzed: keeping the thrust magnitude constant, keeping the thrust coefficient constant, and thrust magnitude computed by table readings with uniform and non-uniform load distribution in the disk.

- ◇ Will there be different results if the upwind distance between the concentrator and wind turbines varies? To clarify if there is a dependency in the position in terrain x of the current concentrator design, three upwind distances x are tested based on the height of the concentrator h: 2h, 4h, and 7h.

- ◇ Will the presence of the concentrator affect negatively the neighbor turbines that are not concentrated? The wind power capacity of these will be monitored in each case.

Finally, the sum-up of the answers to the previous points will lead to a conclusion of the concentrated model of Shagaya Renewable Park.

The study case of the Shagaya Renewable Park is constrained to the following assumptions for all the simulations performed: neutral atmospheric inflow in steady-state condition and driven by shear, fixed concentrator geometry, alignment of the concentrator parallel to

the wind farms rows and inflow perfectly perpendicular to this orientation and final, wind turbines are modeled by the actuator disk theory with only considering normal loadings (no rotational forces are applied). The turbulence model used in all simulations was the $k - \varepsilon - f_P$ model (van der Laan, Réthoré, et al., 2015).

The present research is structured in four chapters and conveys the reader from a literature review, through a review of the model approach up to the analysis of results and final remarks.

Chapter 1, provides a literature review on topics of steady-state RANS approaches on atmosphere modeling in the surface layer and, actuator disk modeling. These topics are reviewed and some open points are elaborated to fund the basis of the model. In the last part, a review of the existing literature on the concentrator's use and the limitations of the theory is discussed.

Chapter 2, introduces general information about the case study, defines the objectives of the present research, and presents the numerical set-up and validation cases that will fund the model to be used later.

Chapter 3, focuses on the pre-processing tasks on the Shagaya study case and covers the description of the numerical set-up, wind turbine's data, key parameters for analysis, the cases that will be studied and it closes with a mesh sensitivity study.

Chapter 4, provides the results and analysis of performing different actuator disk implementations on the three distances set to be studied to finally lead to an analysis of the obtained changes in wind power capacity. Later is the Conclusion section where general remarks and future work recommendations will be provided and the final section, the Appendix.

Chapter 1

Theorethical framework

1.1 ABL modeling

Any wind farm, skyscraper, or tall structure is inside the Atmospheric Boundary Layer (ABL), also called Planetary Boundary Layer. This is the lowest region within the atmosphere, contained between its top by the free stream wind and the Earth's surface at the bottom. The depth of this layer and the wind profiles inside it are directly influenced by the pressure gradients happening in the free stream and the local climate conditions with the surface characteristics of a given location. This layer can also be divided into two sections: just over the surface, the Atmospheric Surface Layer (ASL) and, above this latter up to the free stream, the Ekman Layer.

For modeling the external aerodynamics of any structure inside the ABL it is convenient to take into account what type of stratification the site has at a given time since it will define the vertical profiles of wind velocity and temperature of the study case. For these, there are three main stratification levels to be considered: stable, unstable, and neutral as defined in (Monin & Obukhov, 1954). From this theory, commonly refer as MOST, the vertical wind velocity profile, $u(z)$, and the vertical temperature profile, $T(z)$ can be defined by the following expressions:

$$u(z) = \frac{u_*}{\kappa}\left[\ln\frac{z}{z_o} + \beta\frac{z}{L}\right] \tag{1.1}$$

$$T(z) - T(z_o) = T_*\left[\ln\frac{z}{z_o} + \beta\frac{z}{L}\right] \tag{1.2}$$

Where z is the height level to be evaluated, u_* is the frictional velocity that can be used

as an indirect reference of the intensity of turbulence in the media, z_o is the aerodynamic roughness length which can be either defined as an attribute of the terrain's surface or as profile fitter, L is the MOST length scale and T_*, the temperature length scale and finally β, a fitting constant.

A common practice in CFD community is to model the ABL as neutral stratification, which implies $L \to \infty$ leading to a short version of (1.1) as:

$$u(z) = \frac{u_*}{\kappa}\left[\ln\frac{z}{z_o}\right] \tag{1.3}$$

Which is the log-law profile used in (IEC, 2005) for wind turbine design. Additionally, the vertical profile of temperature is assumed to be constant, which leads (1.2) to zero and neglecting any buoyancy effect.

1.1.1 Turbulence model

Due to the chronological order of turbulence model publications and their availability in CFD development, the $k-\varepsilon$ (Launder & Spalding, 1974) has been one of the first turbulence models to be used and adapted to ABL modeling. This two-equations eddy viscosity model is defined by these transport expressions of turbulent kinetic energy, k, and the dissipation rate ε:

$$\frac{\partial(\rho k)}{\partial t} + \frac{\partial(\rho u_i k)}{\partial x_i} = \frac{\partial}{\partial x_j}\left[\left(\mu + \frac{\mu_t}{\sigma_k}\right)\frac{\partial k}{\partial x_j}\right] + P_k - \rho\varepsilon \tag{1.4}$$

$$\frac{\partial(\rho \varepsilon)}{\partial t} + \frac{\partial(\rho u_i \varepsilon)}{\partial x_i} = \frac{\partial}{\partial x_j}\left[\left(\mu + \frac{\mu_t}{\sigma_\varepsilon}\right)\frac{\partial \varepsilon}{\partial x_j}\right] + C_{\varepsilon 1}P_k - C_{\varepsilon 2}\rho\frac{\varepsilon^2}{k} \tag{1.5}$$

The first term in the left-side hand of both (1.4) and (1.5) represents the rate of change of k and ε over time and, the second term refers to the transport of these by advection. The first term in the right-side hand represents the transport of k and ε by diffusion followed by the terms production of k (P_k). Finally, the last terms correspond to the destruction of these entities. Here, ρ is the density of the fluid, μ is the fluid's viscosity, μ_t is the turbulent eddy viscosity that is an attribute of the flow, and the non-dimensional numbers of the model: the turbulence kinetic energy Prandtl number σ_k, the turbulence dissipation Prandtl number σ_ε, and the constants $C_{\varepsilon 1}$ and $C_{\varepsilon 2}$.

As seen previously, there is an added source of diffusion μ_t, besides the molecular viscosity,

which explicitly depends on the velocity gradient and the length scale l_m of Prandtl's mixing length theory:

$$\mu_T = \rho l_{\max}^2 \left| \frac{\partial u}{\partial y} \right| \tag{1.6}$$

As explained in Apsley and Castro (1997), in boundary layer flows (such as is ABL) the mixing length serves as a reference of the possible range of sizes of eddies, it can also be defined as:

$$l_m = \kappa z \tag{1.7}$$

As for $k-\varepsilon$ model, by dividing by ρ the dynamic turbulent eddy viscosity μ_T, the expression of (1.6) can be rewritten first based on l_m, on the cross-stream velocity fluctuations u', and also on the turbulent variables k, ε thanks to a proportional constant:

$$\begin{aligned} \nu_T &= u' l_m \\ &= C_\mu \frac{k^2}{\varepsilon} \end{aligned} \tag{1.8}$$

Where the eddy viscosity constant C_μ, is another characteristic constant on the $k-\varepsilon$ model.

Even today, the $k-\varepsilon$ turbulence model remains a commonly used approach for simulating ABL, whether the terrain is flat or complex. It's worth noting that while this model persists in use, it's typically accompanied by adjustments to the values of its constant parameters. A first recommendation of a new set of constants values is introduced by Panofsky and Dutton (1984), followed by other researchers as shown in the following table 1.1:

Table 1.1: Constants for $k-\varepsilon$ turbulence model

Authors	C_μ	$C_{\varepsilon 1}$	$C_{\varepsilon 2}$	σ_k	σ_ε	κ
(Launder & Spalding, 1974)	0.090	1.440	1.92	1.00	1.30	0.41
(Panofsky & Dutton, 1984)	0.033	1.176	1.92	1.00	1.30	0.40
(Bechmann et al., 2007)	0.030	1.210	1.92	1.00	1.30	0.40
(Cindori et al., 2018)	0.044	1.440	1.92	1.00	1.67	0.41

As it could be noticed, by adjusting the value of C_μ, proportionally will the eddy viscosity ν_t be adjusted. On the other side, changing the values $C_{\varepsilon 1}$ and $C_{\varepsilon 2}$ will interfere with the production and destruction of turbulence. All these sets satisfy the following condition to reproduce a homogeneous ABL, as set by Richards and Hoxey (1993):

$$\sigma_\varepsilon = \frac{\kappa^2}{C_{\varepsilon 1} C_{\varepsilon 2} \sqrt{C_\mu}} \tag{1.9}$$

It's well known that the $k-\varepsilon$ model has its limitations for predicting velocity gradients in wind farm modeling. This creates a need to find a suitable RANS model that better recreates the wind speed deficit in the wakes of wind turbines along with an ASL inflow.

A new model contribution is made by van der Laan, Réthoré, et al. (2015), named $k-\varepsilon-f_P$ model, which derives from $k-\varepsilon$ model with the new feature of having a non-constant value of C_μ. The eddy viscosity will then be calculated from the C_μ and the limiter function f_P. The f_P is based on the local velocity gradient and a nonlinear function with a calibration constant present as introduced below:

$$\nu_T = f_P C_\mu \frac{k^2}{\varepsilon} \tag{1.10}$$

$$f_P(\sigma/\widetilde{\sigma}) = \frac{2 f_0}{1 + \sqrt{1 + 4 f_0 (f_0 - 1)(\frac{\sigma}{\widetilde{\sigma}})^2}}, f_0 = \frac{C_R}{C_R - 1} \tag{1.11}$$

Where $\sigma \equiv \frac{k}{\varepsilon}\sqrt{(U_{i,j})^2}$ is the shear parameter computed from the local velocity gradient of the flow, and $\widetilde{\sigma} = 1\sqrt{C_\mu}$, hence f_P is also a function of C_μ. The calibration constant C_R is assigned to the value of 4.5 after calibration of the current model against LES simulations (van der Laan, Réthoré, et al., 2015).

Recalling (1.10), the function f_P works as a length limiter that, in combination with its definition, creates a nonlinear eddy viscosity model less dissipative in high shear flow compared with the original $k-\varepsilon$ model, (van der Laan, Réthoré, et al., 2015).

The $k-\varepsilon-f_P$ model uses the same transport equations for k and ε that $k-\varepsilon$ model.

The set of constants of this model are:

Table 1.2: Constants for $k-\varepsilon-f_P$ turbulence model

C_R	C_μ	$C_{\varepsilon 1}$	$C_{\varepsilon 2}$	σ_k	σ_ε	κ
4.5	0.030	1.210	1.92	1.00	1.30	0.40

It will be the choice for incoming simulations to test the $k-\varepsilon$ model and $k-\varepsilon-f_P$, prioritizing the use of this latter in the final study. The set of constants used by van der Laan, Réthoré, et al. (2015) will be also applied to the $k-\varepsilon$ model.

1.1.2 Boundary conditions

For modeling a neutral homogeneous ASL driven by shear, the following options for boundary conditions are considered:

Inlet

As for the inlet boundary conditions the following profiles proposed by Richards and Hoxey (1993) can be used implemented:

$$u(z) = \frac{u_*}{\kappa}\left[\ln\frac{z+z_o}{z_o}\right] \tag{1.12}$$

$$k = \frac{u_*^2}{\sqrt{C_\mu}} \tag{1.13}$$

$$\varepsilon = \frac{u_*^3}{\kappa(z+z_o)} \tag{1.14}$$

With known characteristic values of the site and flow: a wind speed u value at a certain height z, the characteristic terrain's surface z_o and using the set of constants of the turbulence model discussed in section 1.1.1, these vertical profiles can be defined.

The turbulent kinetic energy k is modeled as a fixed value along the vertical profile. A vertical straight profile does not match with experimental data seen in Yang et al. (2009), Yan et al. (2015) and Ricci et al. (2020). The expression for k developed by Yang et al. (2009), which draws a non-constant profile, relies on empirical fitting constants that must be determined depending on each study case. Therefore, for simplicity of use, an acceptable practice nowadays is to implement (1.13) as an inlet condition for shear-driven flows despite this mismatch.

If the incoming wind velocity profile $u(z)$ is a perturbed flow, which means, the profile does not fit entirely with the given z_o of the terrain's surface, then a hybrid profile can be defined from separated profiles of different z_o values that intercepts at certain height points and finally reproduce the irregular incoming wind profile desired, as explained in Marciotto and Fisch (2013). It is worth noting that this type of condition won't result in a homogeneous ABL since the incoming profiles are not in balance with the site roughness length z_o, instead, the output solution in a case like this will be a developing flow seeking equilibrium.

Outlet

The flow is treated as a pressure-outlet velocity flow (Hargreaves & Wright, 2007), which implies a zero value on the kinetic pressure at the outlet, and as for the rest of variables, a Neumman condition of zero gradient.

Laterals

As suggested by Franke and Baklanov (2007), lateral patches can be assigned as symmetry walls, imposing a parallel flow to these by equating to zero the transverse component of the velocity vector. This tends to create a speed-up of the flow at these patches, therefore, it's advisable to follow the guidelines of domain sizing also recommended by Franke and Baklanov (2007).

In contrast, if there are limitations on how long can be width of the domain be, it's possible to replace the symmetry boundary condition with a periodic boundary condition and shorten the distance between object and the lateral patches as seen in Bechmann et al. (2007) and van der Laan et al. (2021).

Top

Firstly, a recommendation of placing a constant shear at this patch is given by Richards and Hoxey (1993). Other researchers have used either symmetry or slip boundary condition, seeking to model a free flow at that patch (Ricci et al., 2020; Richards & Norris, 2011; Yang et al., 2009). This last method has the inconvenience of not fully maintaining the velocity log-law profile at the surroundings of the patch and, recent practices are to assign a fixed value at the top, taken from the log-law inlet profile (Blocken et al., 2007; Cindori et al., 2022). This last is also implemented in the turbulent variables.

Bottom

The lowest patch, z=0, here and after also named as *ground*, must be treated as a rough surface with the use of z_o as indicated by Richards and Hoxey (1993). For this purpose, the specific production of kinetic energy G_k must be in balance (be equal) with the dissipation

ratio, ε at the first cell centroid:

$$\begin{aligned} \varepsilon_w &= G_k \\ \frac{C_\mu^{0.75} k^{1.5}}{\kappa(z_p + z_o)} &= \frac{\tau_w^2}{\rho \kappa C_\mu^{0.25} k^{0.5}(z_p + z_o)} \end{aligned} \tag{1.15}$$

As for the rest of the variables, zero gradient for k and a no-slip condition for the velocity vector.

A common issue known in the field with this current implementation is a peak in k due to a numerical imbalance between ε and G_k regardless of the previous attempt of defining them as the same. The overproduction of k happens in the first cell centers as seen by Hargreaves and Wright (2007) and Parente et al. (2011), something unavoidable by the current method but does not limit its application.

1.1.3 Walls and y+

In external flow modeling with the presence of walls, the mean velocity profiles are affected by the shear stress exerted by the fluid on the wall due to friction, τ_w (Pope, 2000). At the wall nearby, viscous scales are defined in both velocity and length, such as the friction velocity $u_t \equiv \sqrt{\frac{\tau_w}{\rho}}$, and the length scale $\delta_v \equiv \frac{\nu}{u_t}$, where ν is the kinematic viscosity of the fluid. Based on previous scales and considering any orthogonal distance to the wall, such as a characteristic length δ or any other distance y, these new dimensional numbers of the flow can be formulated: the friction Reynolds number Re_t in eq. (1.16) and, the non dimensional number of $y+$ in eq. (1.17):

$$Re_t \equiv \frac{u_t * \delta}{\nu} \tag{1.16}$$

$$y+ \equiv \frac{u_t * y}{\nu} \tag{1.17}$$

It is noticed that both Re_t and $y+$ share the same formulation, so it's expected that the $y+$ value provides information on how viscous and turbulent processes occur in the nearby walls, being $y+$ a key variable in CFD modeling near walls since the choice of boundary conditions depends on the approximated values obtained of $y+$ at the center of the first cell adjacent to a wall.

By definition on (1.15), this wall function has no dependency in y+ of the first cell, giving

some freedom to assign larger first cell heights outside the meshing standard on boundary layer flows. The choice of first cell height may vary within the range of the same order of z_o as chosen by van der Laan, Réthoré, et al. (2015), a choice of 0.5 m height as seen in van der Laan et al. (2021), even up to 1 meter of height as chosen by Hargreaves and Wright (2007). A comparison between meshing complex terrain with 1 m cell height from a 0.025 m cell height mesh finds that the coarser mesh had a numerical deviation of $4 * 10^{-3}$ on wind speed velocity (Gargallo-Peiró et al., 2018).

In Hågbo and Giljarhus (2022) was discussed the challenge of meshing with small cells height at the walls at high Reynolds number for study cases of rough terrain, in their specific case, a study of urban area for pedestrian comfort. In this type of wind energy study, the minimal requirement on the local mesh is to ensure 3 cells contained in 2 m height to catch the wind flow for pedestrian comfort analysis (Franke & Baklanov, 2007). Even though it was seen y+ within 7000 to 9000 for buildings and immediate ground area, and higher values in the next research of $y+$ between 4.510^4 and 7.510^4 (Hågbo et al., 2021). Similar values were found by Hargreaves and Wright (2007) and Venkatraman et al. (2023) in their research. It leaves uncertainty if the precise modeling of the near wall may importantly impact accuracy in measurements in areas of interest far from the wall. As pondered by Hargreaves and Wright (2007), a standard for y+ for ABL flows is likely necessary for the field.

1.2 Actuator disk modeling

Due to computational expenses, it is a preferable choice to model the interaction of a Wind Turbine (WT) with the flow, rather than resolving the complete turbulent flow over a rotating 3D geometry. This last procedure will always require high-quality mesh and low $y+$ at walls to guarantee well-resolved physics. In the review of the literature of the present project, only a few publications resolving complete 3D rotating blades were found: for FSI and aeroelastic analysis (Grinderslev et al., 2021), in wind tunnel validation (Enger, 2018; Zhang et al., 2019), for power performance in flat terrain (Réthoré et al., 2014) and in complex ones (Schulz et al., 2014).

The simplest method of modeling a WT is by the implementation of an Actuator Disk Model (ADM). This method is based originally on 1-D dimensional momentum theory

(Manwell, 2009) and consists of a prescribed force applied over a disk area/volume, where the following assumptions are made: homogeneous, incompressible, steady state fluid flow; no frictional drag, infinite number of blades, uniform thrust over the disc, a non-rotating wake and, the static pressure far upstream and far downstream is equal to the undisturbed ambient static pressure. This theory ends up relating the undisturbed reference wind velocity U_∞, usually, this one is measured at hub height far upstream, with the wind velocity read at the center of the disk, U_d, by an induction factor α as shown below:

$$\alpha = 1 - \frac{U_d}{U_\infty} \tag{1.18}$$

The force exerted by the wind turbine on the wind is called thrust, T, and from this, there is a non-dimensional thrust coefficient. Both relate to the previous variables in (1.18) by:

$$T = 0.5\rho A U_\infty^2 [4\alpha(1-\alpha)] \tag{1.19}$$

$$C_T = \frac{T}{0.5\rho A U_\infty^2} = 4\alpha(1-\alpha) \tag{1.20}$$

Where ρ is the air density and A is the swept area of the rotor. Similarly to thrust, there are definitions for the power output P and the corresponding power coefficient, C_P:

$$P = 0.5\rho A U_\infty^3 [4\alpha(1-\alpha)^2] \tag{1.21}$$

$$C_P = \frac{P}{0.5\rho A U_\infty^3} = 4\alpha(1-\alpha)^2 \tag{1.22}$$

Finally, both (1.19) and (1.21) can be rewritten using the C_T and C_P tabulated values of a given model of WT:

$$T = 0.5\rho A U_\infty^2 C_T \tag{1.23}$$

$$P = 0.5\rho A U_\infty^3 C_P \tag{1.24}$$

Now, the incoming question is how this method has been implemented in CFD for a single turbine and wind farm study in recent years.

1.2.1 ADM approaches

As seen in Cabezón et al. (2009), the ADM is a cylindrical array of cells grouped where a sink term is to be applied at the cell center of them. The sink term, at its basics, is the thrust force magnitude from (1.23) with the rest of known variables: U_∞ which is the undisturbed wind velocity at hub height, C_T corresponds to the value read in WT's curves and A from the rotor's diameter, D. Note that for some incompressible solvers such as simpleFoam in OpenFOAM, the dependency in ρ is omited.

A big challenge found in earlier RANS simulations happens when using standard isotropic turbulence models, such as $k-\varepsilon$, $k-\omega$ and derivations of them, as $realizable k-\varepsilon$ and $k-\omega SST$, the near wake of the ADM could not reach enough wind speed deficit to match with field measurements. Research of Cabezón et al. (2009) and Cabezón et al. (2011) have tested the anisotropic Reynolds Stress Model, RSM, and proven to get good matches with experimental data but still, RSM is not a popular model choice in the wind energy sector and keeps being in the state-of-the-art (Cabezón, 2013).

Some researchers have chosen to design variants of $k-\varepsilon$ by adding source terms to the turbulent fields, k, and ε along with the momentum sink. These new source terms are applied inside a larger disk than the current ADM (where the momentum sink term is applied). Some examples of this type of approach are the models from Kasmi and Masson (2008), Réthoré et al. (2009), Ren et al. (2019) and Ning et al. (2021). All of them show good matching with experimental data, but, also share in common that all of them are tests of single isolated turbines in flat terrain with dependency on empirical constants. This type of WT modeling has not been seen implemented either on a real-scale wind farm, either in flat terrain or in complex terrain. This generates uncertainty if other researchers have not found this modeling approach feasible to use in wind farms.

The choice of the author to improve near wake predictions in RANS CFD is the use of $k-\varepsilon-f_P$ (van der Laan, Réthoré, et al., 2015), introduced already in the previous section 1.1.1. This approach skips any requirement of additional sources, aside from the momentum sink of the thrust exerted by the turbine. In addition, it skips the pre-processing steps on creating new sets of cells where these turbulent sources are applied. Researchers that have used previously this model are Navarro et al. (2018) and Hardy (2017), and found satisfactory the performance of this model. More advantage that the author finds on $k-\varepsilon-f_P$, is that at the present date, the state-of-the-art keeps expanding

for modeling interaction between wind farms and non-neutral ABL.

1.2.2 Load distribution in disk

The prescribed magnitude force from (1.23) may be distributed in several ways over the disc (Simisiroglou et al., 2017). The most commonly used is uniform load distribution which consists of weighted thrust contributions over the cells according to their volume, obtaining a constant value of thrust applied along the radius of the ADM. This load distribution is either used in RANS as seen in Cabezón et al. (2009), Gargallo-Peiró et al. (2018), Ávila et al. (2017) and Navarro et al. (2018), as in LES simulations such as Calaf et al. (2010), Tobin and Chamorro (2017) and Liu and Stevens (2021).

A point to consider from Simisiroglou et al. (2017) is that in real-scale wind turbines, the thrust at the hub and blade's tip is zero. This can be modeled by implementing a prescribed load profile or a polynomial function load distribution. For this method, there is a big limitation for the industry in having detailed aerodynamic data of the airfoils to apply the Blade Element Method theory and find the flow-dependent load distribution along the blades. Some remedies for this are to compute a polynomial distribution by choosing an order for the polynomial (Réthoré et al., 2014), another option is to use a normalized load profile from an aeroelastic software (using the most similar generic wind turbine model of their database), or finally, by copying a known load distribution from another WT model, that as could be presumed, leaves the uncertainty if the load distribution matches with the exact airfoil of the case of study. Research done by using these types of distributions are found in Kasmi and Masson (2008), Javaheri and Cañadillas (2013), Réthoré et al. (2014), van der Laan, Réthoré, et al. (2015), Ren et al. (2019), Sørensen et al. (2020), van der Laan et al. (2023) and Hamlaoui et al. (2023).

Open points

The vertical wind velocity profile differs if solved as nonuniform-loaded or as a uniform-loaded rotor. In the first, there is no thrust applied on the hub so no velocity drop will be found in this point, different from the uniform loaded disk that does. This can be easily verified in axial velocity contour plots from the research cited before. It's presumed that this difference inside the rotor disk when using one distribution or another, may resolve differently the flow interactions when an upwind perturbation goes into the WT.

Besides differences in hub values and vertical wind velocity profiles between distribution methods, both have been validated against experimental data of wind farm power deficit. It's noted that most 'measurements' and 'experimental data' are expressed as scaled values to ease comparisons, and what is commonly pursued is to validate the ratio of changes in wind speed or power production between a single WT with another, or a row against another. By this, it can be assumed that both methods can predict ratios of changes satisfactorily but is not guaranteed that they predict correctly absolute values (e.g., the wind speed in metric units at certain point of the rotor modeled).

One more point to discuss is the casual consideration of the nacelle contribution on the ADM and wake. It is worth clarifying that (1.23) is mainly thrust exerted by the blades and the distributions discussed in section 1.2.2 only considered this force. A nacelle drag contribution could be considered aside, by assumptions of drag coefficient between 0.8 and 1.2 given in Kasmi and Masson (2008), Ren et al. (2019) and Ning et al. (2021), but there are no clear guidelines given on how to choose this coefficient for existing WT's nacelle.

1.2.3 Wake-affected turbines

There are clear guidelines on what values to prescribe for isolated wind turbines in flat terrain, but as for those wind turbines that are either isolated in complex terrain or, placed just after a row of turbines, it is difficult to identify a unique set of parameters values to prescribe the thrust magnitude on them. Several studies have been performed to address the way of handling wake-affected WTs.

Earlier methods

As explained Politis et al. (2012), the first approach to solving wake-affected turbines was to first simulate an empty domain with the ABL parameters and gather readings of hub velocity, then, launch a new simulation with the thrust prescribed in the ADM based on the measurements, and if there were more WT downstream, repeat by stages this method until all rows are covered. This method does not promise accuracy and leads to too much work for the user. The next solution was to make an iterative process over the induction factor until convergence was reached. For that, the solution will be space dependent since it requires reading a representative value for U_∞, usually set as a hypothetical hub point

or average disk value 1.5D (Cabezón, 2013) and along with the local reading of U_d, find α. The calculation of $C_T = f(\alpha)$ is defined by two expressions according to the value of α (Politis et al., 2012).

Fixed thrust coefficient method

Here is presented the corrector of thrust coefficient, C'_T (Calaf et al., 2010) which is defined as:

$$C'_T = \frac{C_T}{(1-\alpha)^2} = \left(\frac{U_\infty}{U_d}\right)^2 C_T \tag{1.25}$$

The solution for wind farm modeling that Calaf et al. (2010) designed was to set the same thrust coefficient C'_T for all the wind turbines of the farm and reformulate (1.23) now as:

$$T = 0.5\rho A U_d^2 C'_T \tag{1.26}$$

Where U_d is now defined as the average disk value and U_∞ is the undisturbed wind velocity at hub height from the inlet.

Tabulated calibration

Novel methods were introduced by van der Laan et al. (2014) and Navarro et al. (2018) based on tabulated input data into the ADM, from a calibration procedure. Both strategies require a range of wind speed simulations, e.g. $4 \leq U \leq 22$ [m/s] in intervals of 1 m/s, on a single isolated wind turbine with the same characteristic of ABL that the final case study. From each wind speed simulation, there must be extracted the average disk value U_d. A table then can be either elaborated by matching the U_∞, $C_T(U_\infty)$ and U_d (Navarro et al., 2018) or, U_d with C'_T (van der Laan et al., 2014). This tabulated data must be used for the querying task of the ADM on each reading U_d and auto-correct the thrust magnitude to be applied either by (1.23) or (1.26). Both procedures end on a non-fixed thrust coefficient in the wind farm and in auto-corrected thrust force magnitude, which could be associated with an 'automated controller' on the wind turbine.

The methods by Calaf et al. (2010) and Navarro et al. (2018), in the next section refer as CA and CC & NC methods, will be tested in the following chapters.

1.3 Windbreaks

Windbreaks are artificial structures that can be built as solid or porous surfaces. Its most common use is for wind protection of harvest, passages, and others. The performance of a windbreak depends on conditions of ABL, wind direction, and proper characteristics of the structure (e.g. dimensions, aspect ratio, porosity). Here, the Reynolds number R_e, can be computed based on horizontal wind speed U_h read at the top height h of the windbreak, $R_e = \frac{U_h * h}{\nu}$, where h also works as characteristic length (Fang & Wang, 1997). As the flow approaches the windbreak, the streamlines are lifted and create a speed-up region just above the windbreak's tip. A separation of the flow starts at the tip of the windbreak and the reattachment to the surface and its recovery it's dependent on the porosity and height of the windbreak. The turbulence generated on the downstream flow by the windbreak depends on the representative scale of h/z_o and the stratification of the ABL (Heisler & Dewalle, 1988).

Many other research has been performed to understand how the wind flow behaves in the presence of windbreaks to find optimal wind speed reduction downstream. The focus in the present project is the opposite, here is pursued the speed-up zone created at heights above the windbreak's top.

1.3.1 Windbreak models on windfarms

An introduction in windfarm design of placing windbreaks in the nearby of a WT is given by Tobin et al. (2017). The turbulent flow may be characterized by a velocity scale U_h (defined before) and the vertical mixing length scale $l(x)$ which depends on the local lee position inside the recirculation zone (Tobin et al., 2017, Fig 1). A wind tunnel experiment was conducted for three porous windbreaks prototypes of $\eta = 0.1$, and height ratios $\frac{h}{z_{hub}}$ of [0.1, 0.15, 0.2] located $5h$ upfront of a first WT prototype. A second WT prototype is placed 10D downwind, also with windbreak. The inflow length scales h/z_o were [1700, 2550, 3400] with R_e [7200, 11000, 14000] on each case. An additional turbulence scale in the form of a Reynolds number is defined to ensure dynamic similarity between prototypes:

$$Re_{turb} = \frac{1}{\sqrt{\kappa}} \ln \frac{h}{z_0} \tag{1.27}$$

Which results for the experiment $Re_{turb} = 40 \pm 1$.

To evaluate the changes, a ratio between power production without windbreak P_0, and the net power increase ΔP is defined below:

$$\frac{\Delta P}{P_0} = \frac{(U_{hub} + \Delta u)^3}{U_{hub}^3} - 1 \tag{1.28}$$

Results came with $\frac{\Delta P}{P_0}$ of [0.08, 0.14, 0.19] for the prescribed $\frac{h}{z_{hub}}$ range tested. A linear theory was developed after, to relate the height of the windbreak with the increase in wind power production:

$$\frac{\Delta P}{P_0} = \alpha_c \frac{h}{z_{hub}} - \beta_c \tag{1.29}$$

Where α_c and β_c are fitting constants of the model (Tobin et al., 2017, Table 4).

Despite the optimization on the first wind turbine, when h/z_o = [2550, 3400] the second wind turbine reported a drop in wind power production by 2.4% and 11.4% accordingly. An open question was left on the downwind changes.

Next research effectuated by Tobin and Chamorro (2017) is a real-scale LES simulation of windbreaks within infinite wind farms, to evaluate specifically what happens in downstream rows with the presence of windbreaks, based on the previous results in Tobin et al. (2017). A hypothetical wind turbine of $z_{hub} = D = 100m$ was set as porous ADM with a prescribed $C_T' = 0.9$ to apply on the force thrust from (1.26). Windbreaks of length $b = 2D$ and heights of $\frac{h}{z_{hub}}$ 0.12 and 0.2 were modeled as porous media as:

$$F_{wb} = -0.5\rho k_n U_d^2 bh \tag{1.30}$$

where k_n is a screen-pressure coefficient. Here was again assigned a fixed upwind distance of $5h$ between windbreak and WT. The study case results showed a drop in wind power production for distances between rows lower than 500D. If a hypothetical second row at 'infinity distance' (reference for a single-row wind farm), an enhancement in $\frac{\Delta P}{P_0}$ is found positive and grows up as porosity decreases in the windbreak.

Linked to the first windbreak on wind farms study, a new wind tunnel experiment was conducted. A set of 100 porous models of WT arranged as 20x5 matrix, with stream wise separation of 7D were tested, with and without scaled windbreaks of $\frac{h}{z_{hub}}$ 0.12 and 0.2. As a result, an overall drop of 5% to 10% in estimated power production was obtained .

In contrast, the next research provided by Liu and Stevens (2021) finds positive $\frac{\Delta P}{P_0}$ on

multiple row wind farms by making some modifications on the initial work of Tobin and Chamorro (2017). First to note is that they tested several upwind distances x_t along with $\frac{h}{z_{hub}}$. Second, the porosity tested drops up to $\eta = 0.03$. Third, the length of the windbreak is also varied from 2 to 5 times D. They intend to reproduce the same ABL conditions than Tobin and Chamorro (2017) in a LES simulation, also replicating the same wind farm array with ADM using $C_T' = 0.9$, in addition with a windbreak modeled as a porous barrier. Promising configurations now are found by extending x_t or shortening x_t with a taller windbreak on a complete multiple-row wind farm. First row with windbreaks increases $\frac{\Delta P}{P_0}$ upto 40%, and rows downstream experiences $\frac{\Delta P}{P_0}$ from 5% upto 15%.

1.3.2 Literature limitations

The most important limitation is that there are no documented field experiments (real scale) measurements of windbreaks placed the near upfront of a wind turbine to validate any CFD model. This creates an impediment to the evaluation of the accuracy of the results gathered.

It is worth pointing out and recalling comments in 1.2.2, that both Tobin and Chamorro (2017) and Liu and Stevens (2021) follows Calaf et al. (2010) procedure on ADM, which consist of fixed corrected C_T coefficient, C_T' for all wind turbines and a uniformly loaded distribution in ADM. These two authors are the only ones found to have studied using CFD the performance of windbreaks in wind farms.

On the other hand, the literature research practiced did not find any validation case on how the wind profile develops inside the transition from the undisturbed wind to the actual position of the hub point. As each WT load distribution develops a different vertical velocity profile, it is not clear which load distribution is convenient to test along with the concentrator.

As per possible theoretical estimations in wind power production, eq. (1.29) has limitations since partially considers some characteristics of a case setup. This linear relation only accounts for porosity and height ratios but does not have a kind of correlation with ABL conditions nor upwind distance from concentrator to turbines.

Chapter 2

Methodology

In the present chapter will be presented a description of the study case, the objectives pursued, the generic set-up of the simulations, and cases of validation by similarity of the models to be combined in the future stages.

2.1 Project description

2.1.1 W'wave

Winnowave SL (W'wave) is a clean technology company pioneer in the technology of concentrating wind. Their proposal to the wind energy industry is to artificially accelerate the wind with the use of 'concentrators' for the benefit of increasing power production in the wind turbines and therefore, as a consequence help to lower the costs of the energy. They ran the first experimental assessments in 2020 in CEDER-CIEMAT facilities (Ramos, 2020) and successfully acquired the proof of concept for their first built prototype. Currently, they are on the design of a prototype for the Shagaya Wind Project of Kuwait Institute For Scientific Research (KSIR, n.d.).

2.1.2 Shagaya Wind Project

The wind farm chosen for a real-scale study of the performance of a concentrator is the single-row wind farm of Shagaya's Renewable Park of KSIR, Kuwait. The location of the wind farm is 29º13'32"N 47º02'47"E and consists of 5 units of wind turbines SIEMENS GAMESA G97/2MW of IEC class S, aligned in a single row with an inter-spacing of 330

m between turbines. Each turbine has 97 m of the rotor diameter and 79 m of height. The installed capacity of the wind farm is 10MW and is part of a 3.2GW renewable park project of KSIR. The site characteristics can be described as flat terrain with a rough surface characteristic of a desert.

2.1.3 W'wave's proposal

Three consecutive units of the five wind turbines installed are to be concentrated by placing upfront a solid flat rectangular steel-profile compound wall of 810 m in length and 12 meters tall, as fig. 2.1a shows. To later conduct a field measurement campaign in the concentrated and non-concentrated wind turbines, the first three wind turbines from west to east called rotors N1, N2 and N3, are the selected ones to be concentrated and a render view of this subsystem will look like is shown in fig. 2.1b. The optimal upwind distance is to be defined in the present research.

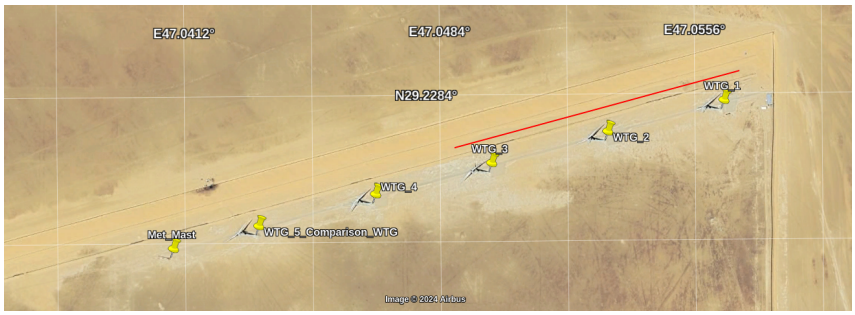

(a) Google Satellite top view. Red line: concentrator's reference. Yellow markers: position of turbines and met mast. ("Google Earth Pro", 2023)

(b) 3D render of the concentrated subsystem (only first 3 turbines are shown) (W'WAVE, 2022)

Figure 2.1: Wind concentrator proposal for Shagaya Wind Project

2.2 Objectives

Evaluate the impact of a high-aspect ratio solid wind-concentrator allocated upfront of three aligned wind turbines G97/2MW from Shagaya Renewable Park in Kuwait within an ASL modeling.

2.2.1 Specific objectives

1. Evaluate the performance of a windbreak along with these 4 cases of actuator disk implementation:

   (a) Prescribed thrust magnitude of the same value as wind turbine without concentrator

   (b) Variable thrust magnitude with fixed thrust coefficient as Calaf's approach, and uniform thrust distribution.

   (c) Variable thrust magnitude based on reading a table with the manufacturer's curve data, and uniform thrust distribution along the disk.

   (d) Variable thrust magnitude based on reading a table with the manufacturer's curve data, and non-uniform thrust distribution along the disk.

2. Determine the optimal distance between options x_t/h: 2, 4 and 7; for the allocation of the concentrator from the hub.

3. Determine if the wind power capacity of the non-concentrated turbines is affected by the presence of the concentrator.

4. Ponderate the net power increase that the Shagaya Renewable Park in Kuwait can achieve due to the installation of the concentrator.

2.3 General numerical setup

In common for all validation cases simulations and project simulations, it has been used the code OpenFOAM ESI V2012. Hexahedral-dominant not-structured meshes have been generated for all the cases via the snappyHexMesh meshing tool.

In connection with the turbulence model $k - \varepsilon - f_P$ in section 1.2.1 and defined within equations (1.4),(1.5), (1.10) and (1.11), it has been used the code implementation from Navarro (2022).

For all the simulations, a discretization of Gauss linear with limiters for the gradients was used, along with a second-order upwind scheme (linearUpwindV) for the velocity flux. For the turbulent convective terms, will be clarified in each following section. The laplacian terms and the surface normal gradients were set to linear limited scheme.

Furthermore, cases have been treated as incompressible flow and solved in steady-state with the SIMPLEC algorithm. Relaxation factors were set to 0.9 for velocity and turbulent fields, and the pressure equation was 1.0. The algorithm used to solve pressure is GAMG and for velocity and turbulent variables the PBiCGStab with DILU conditioner.

All simulations have been set to achieve convergence when residuals reach 10^{-5} and also steady behavior is detected in probes.

2.4 Validation case of ABL flow over building

The case selected for this objective is the experiment conducted by W'WAVE in the facilities of CEDER-CIEMAT, to test the influence on the wind flow of a concentrator prototype called CWPROOF, and predict the power increase. More details on the experiment can be reviewed in Martí (2020) and Ramos (2020).

2.4.1 Domain and mesh

To summarize the case, the geometry consists of the arrangement of six ship containers in three columns to form a "\ _ /" with a rotated orientation of the side columns to the center column of 15º degree, facing the concave inner face upwind. The measurement campaign was held by CEDER with the use of HALO Photonics Lidar system (Ramos, 2020). As the most detailed vertical inflow profile data registered was at a distance of 50 m upfront the concentrator, this distance was used to set the separation between the geometry to the inlet patch of the domain. Still, this distance complies with the general guidelines of 5H for upstream separation Franke and Baklanov (2007).

Sizing of the domain is set to 545x300x240 m following guidelines of Franke and Baklanov (2007) with a 0.3% of Bloackage Ratio (BR), with an initial structured mesh of 96x72x45

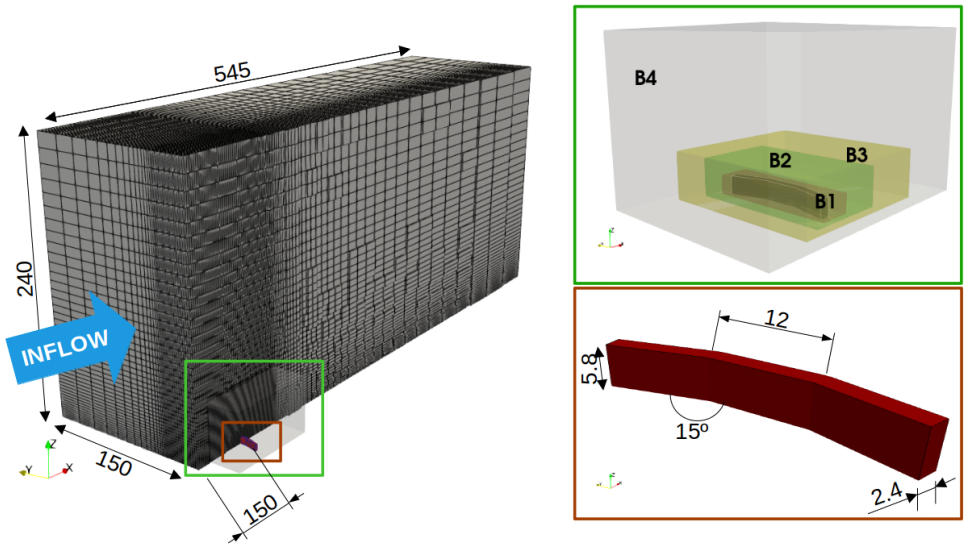

Figure 2.2: Domain and mesh preview (mirror view) of CIEMAT validation case. Green box: refinement regions tested. Red box: close-up of the concentrator design from sea-ship containers

cells as visualized in the half view in fig. 2.2, with a first cell height of 0.5 m. Several tests on different levels of refinements in inner regions as shown in fig. 2.2 close to the concentrator were executed to analyze the mesh sensitivity. The region to monitor convergence is the hypothetical location of a wind turbine of z_{hub} of 25 m and D at a distance of 15 m from the concentrator, of 15 m. This assumption leads to defining a characteristic length of $h/z_{hub} = 0.232$.

The following levels of refinement and regions were executed in three meshes without boundary layer at the concentrator walls and are explained in table 2.1:

Table 2.1: Description of meshes

Mesh	feat.Edges	refSurface	B1	B2	B3	B4	Mesh size (cells)
Mesh 1	3	4	2	1	0	0	431,936
Mesh 2	4	4	3	2	1	1	1,161,126
Mesh 3	5	4	4	3	2	1	4,263,093

2.4.2 Boundary conditions

The vertical inflow profile is a perturbed flow in development since a few meters behind is a canopy of trees and crops. As discussed in section 1.1.2, it can be recreated by a hybrid profile that better fits the data from the joint of two or more profiles varying z_o. The surface roughness of the immediate terrain at the concentrator is characterized by

$z_{o,g} = 0.0025$ m, which leads to defining an additional characteristic length scale of $h/z_o = 2320$ and $Re_{turb} = 12.25$. The inlet profile used follows the expression of:

$$u(z) = \begin{cases} \frac{0.3078}{0.40} \ln \frac{z+z_{o,ug}}{z_{o,ug}} & \text{if } z \leq 10.24 \\ \frac{1}{0.6312} \ln \frac{z}{0.1803} \end{cases} \tag{2.1}$$

This hybrid profile can be set in OpenFOAM with the boundary condition codedFixedValue. For details, please refer to appendix A.2. Similarly, for the turbulence fields, a new matching value of z_o is to be calculated to match with the inlet turbulent intensity TI profile as (1.13). This value was found to be $z_{o,tg} = 0.4788$, and it is to be applied in both (1.13) and (1.14) via the boundary conditions atmBoundaryLayerInletK and atmBoundaryLayerInletEpsilon.

At the top patch, for all fields, a fixed value from the inlet solution was placed except for the pressure which was given a Neumann condition of zeroGradient.

The bottom patch is treated as a rough wall surface in atmospheric flow, so boundary conditions used were noSlip for velocity, for the turbulent viscosity the atmNutkWallFunction with $z_{o,ug}$, wall function for k and, for ε the wall function atmEpsilonWallFunction with $z_{o,tg}$. Finally, for the structure of CWPROOF a noSlip condition for velocity along with wall functions of kqRWallFunction and epsilonWallFunction with a treatment of smooth wall.

For the outlet, kinematic pressure was set to zero and the rest of the variables had an inletOulet boundary condition. Laterals were treated as symmetry patches.

2.4.3 Numerical schemes

As non-orthogonality reached a maximum value of 50^{o}, no additional orthogonal correctors were used with the SIMPLEC algorithm. Second-order upwind was used for turbulent convective terms.

2.4.4 Mesh convergence

At this stage, no boundary layer had been added to the meshes, only the cell size result of the refinement level was left. In fig. 2.3 shows the result of the convergence study.

The velocity monitored was the hub point. The extrapolated solution of the velocity is

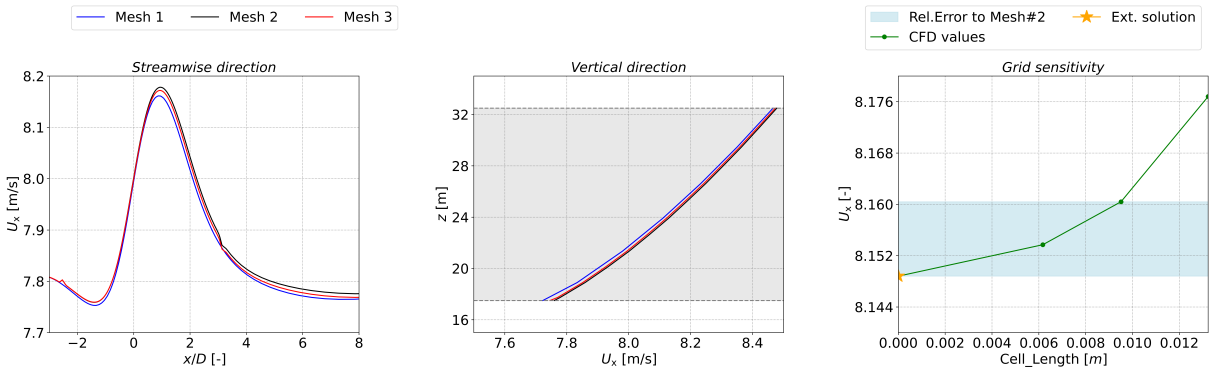

Figure 2.3: Mesh sensitivity convergence.

based on the assumption of the cell volume $vc \to 0$, and lead to a value of 8.148 (m/s). It's seen a monotic convergence with a Richardson order p of 1.99 (Celik et al., 2008) and a GCI index (Roache, 1994) of 0.07% for the fine mesh. On a balance of accuracy vs. expenses, it was chosen Mesh 2 for future analysis, which ends to have a relative error to the extrapolated solution of 0,15%. Mesh 2 has a range of (min/max/average) y+ at the walls of (6.83, 1780.06, 251).

The R_e in this case is 1.710^6 with a concentrator of 5.8 height. By the skin friction approximation on y+, an expected cell height of 0.0026 m should meet with all the cells at the wall below y+ of 300. There is a new trial on remeshing Mesh 2 now with the feature addLayers activated for 12 layers at the wall with cell-to-cell ratio of 1.25. The fig. 2.4 provides a zoom-in view on how the new Boundary Layer (BL) resulted.

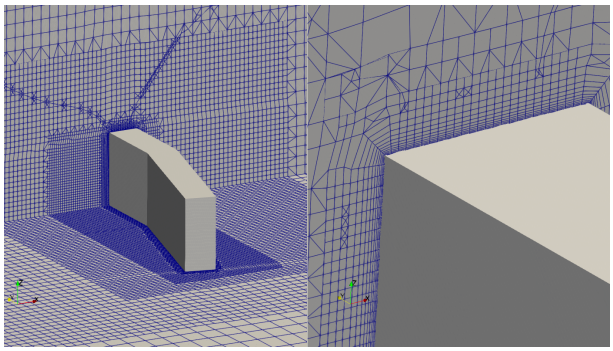

Figure 2.4: Close-up of nearby refinement and boundary layer of concentrator.

Since for some geometries and background meshes, snappyHexMesh tool does not perform well on meshing boundary layer, it's seen as a great opportunity to quantify the error between the absence and presence of well-elaborated boundary layers in the mesh.

An interesting point seen in table 2.2 is that the solution from a mesh without and with BL is that for a target area far from the wall, just as it can be thought the location of a

Table 2.2: Y^+ mesh characteristics

Mesh	Layers	Min	Max	Average	$U_{x_{\text{hub}}}$ (m s^{-1})	Rel. Error (%)
No BL	0.00	6.83	1780.06	251.00	8.16	0.19
With BL	12.00	1.96	108.72	26.37	8.14	–

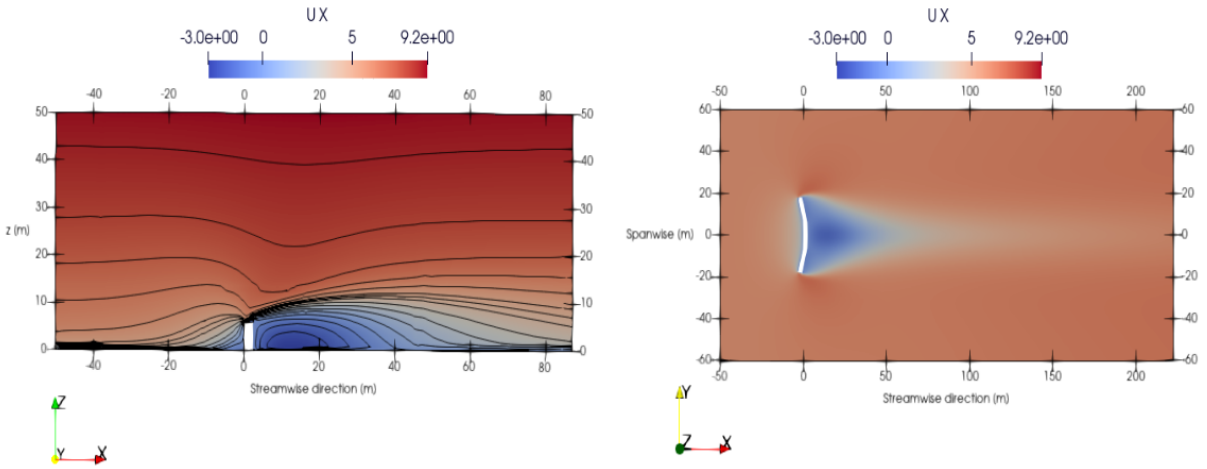

Figure 2.5: Wake contours of horizontal wind velocity of $k-\varepsilon-f_P$ solution. Left: Plane at the center of concentrator with iso-lines of several velocity levels. Right: Plane at half the height of the concentrator.

hub respect to the top of concentrator, the high-detailed resolution of wall characteristics may not have an important influence in the flow inside the rotor. This is worth pointing out since it has been found difficult to model BL in thinner structures.

2.4.5 Results of validation

Two turbulence models were tested: Standard $k-\varepsilon$ and $k-\varepsilon-f_P$ with model constants from table 1.2. In the left contour of fig. 2.5 it can be noticed that upper streamlines decrease in height level creating a speed-up region close to where a wind turbine would be. Additionally is noticed at the right contour that the wake of the concentrator still exists 15h after.

From measurements gathered from a vertical straight line at hub location along the z-axis, the comparison between solutions and experimental data is visualized in fig. 2.6.

A summary between models results is coupled in table 2.3:

Both models agree well with measurements at the rotor region, still by a slight difference $\kappa-\varepsilon-f_P$ has a better agreement that $\kappa-\varepsilon$.

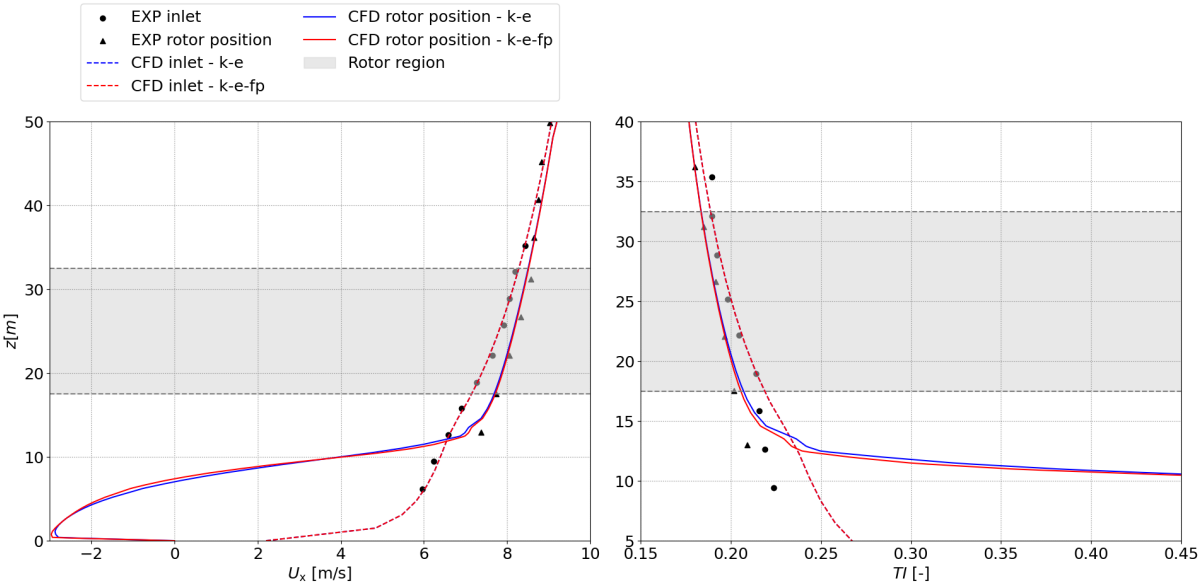

Figure 2.6: Model validation, experimental measurements from Martí (2020)

Table 2.3: $\kappa - \varepsilon$ and $\kappa - \varepsilon - f_P$ comparison at rotor region

	$\kappa - \varepsilon$		$\kappa - \varepsilon - f_P$	
	R^2	Rel. Error (%)	R^2	Rel. Error (%)
Ux	0.999	3.300 %	0.999	0.740 %
TI	0.966	0.890 %	0.972	0.650 %

2.5 Validation case of ADM

It is chosen the case of validation of NREL wind turbine on high turbulent intensity showed in van der Laan, Réthoré, et al. (2015) since it provides measurements for comparison for both wake velocity deficit and wake turbulent intensity from a LES simulation. A summary of the initial conditions is shown in section 2.5:

Table 2.4: Input parameters for numerical computations

Case	z_{hub} [m]	D [m]	U_∞ [m/s]	TI_{hub} [-]	C_T [-]
NREL high TI	90.00	126.00	8.00	12.00%	0.79

2.5.1 Domain and background mesh

The guidelines for domain sizing and mesh discretization follow the guidelines of van der Laan, Réthoré, et al. (2015). The domain elaborated is 25D in stream wise direction, 16D

in span wise and vertical direction leading to a BR of 0.31%. The mesh is hexahedral dominant and non-structured, made only with the blockMesh meshing tool. The actuator disk ADM is placed at the spanwise center of the domain and 5D downstream from the inlet patch as can be observed in fig. 2.7. The group of cells is done via topoSet feature in OpenFOAM. The fig. 2.7 is a representation where the heavier density of discretization

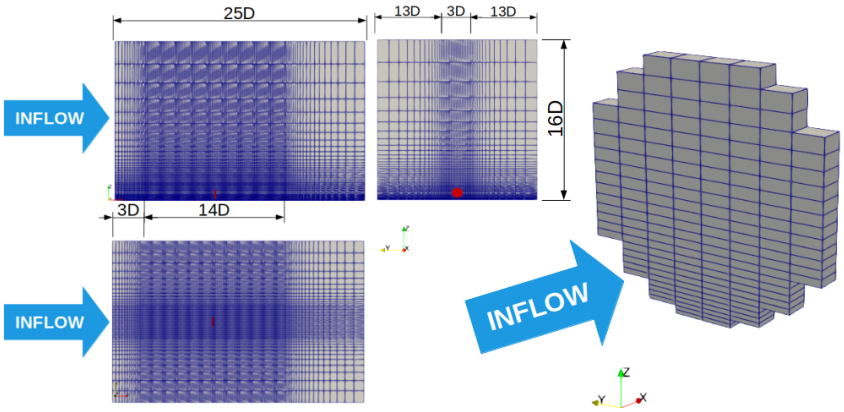

Figure 2.7: Domain dimension and mesh discretization in actuator disk validation. Red marker: cellSet of ADM.

is distributed in the mesh. Several horizontal mesh discretizations were tested as seen in fig. 2.8: 8, 10, 16, 20, and 24 cells per diameter, where the wake discretization goes from 7D upstream the WT up to 7D downstream as shown in fig. 2.7. All the meshes have in common the same discretization in the vertical direction, with a first cell height of 1 m.

2.5.2 Boundary conditions

As the physics involved are of ABL modeling, the same boundary conditions classes applied in section 2.4.2 are been implemented here with the exceptions of:

1. Inlet vertical profiles of $u(z), k, \varepsilon$ are of the same value z_o to model an homogeneous neutral ABL.

2. z_o is calculated from relation between TI_{hub} and z_{hub} (van der Laan, Réthoré, et al., 2015) defined below:

$$TI_{hub} = \frac{\sqrt{\frac{2}{3}k}}{U_\infty} = \frac{\kappa\sqrt{\frac{2}{3}}}{ln\left(\frac{z_{hub}}{z_o}\right)(C_\mu)^{1/4}} \tag{2.2}$$

2.5.3 Numerical setup

For the application of sink terms as an *ADM* in OpenFOAM the fvOption dictionary is used. To discard any under or overestimation of thrust, it is used vectorSourceCode class to implement uniform and non-uniform distribution. For details, refer to appendix A.3. As for numerical schemes, turbulent convective terms were discretized with a second-order upwind scheme.

2.5.4 Mesh sensitivity study

The mesh sensitivity study is performed with the $k-\varepsilon-f_P$ model and there is applied a uniform constant load in the actuator disk. The wake results can be observed in fig. 2.8.

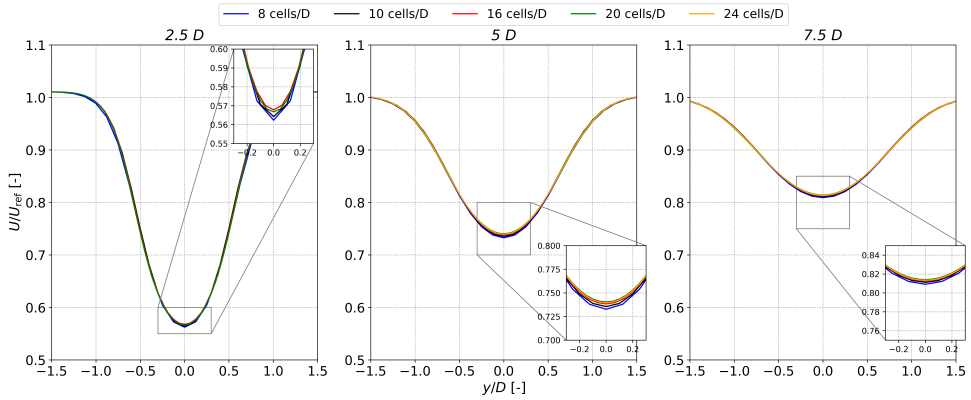

Figure 2.8: Mesh sensitivity study in horizontal-uniform refinement of the wake of the ADM

.

At this stage, by gathering horizontal velocity values at the hub point, a slight non-monotonic pattern in convergence is appreciated in fig. 2.8 and, then verified when computing the extrapolated solution for an infinite mesh as observed in fig. 2.9. It's difficult to ensure the order of convergence when the pattern is non-monotonic while the cell density in the mesh increases. This could be related to an important occurrence of turbulent diffusion in the physics involved in the wake. Looking for a balance between accuracy and computational expenses and, a lower relative error to the extrapolated solution, the uniform wake discretization of 10 cells/D is chosen for further studies.

Despite that in van der Laan, Réthoré, et al. (2015) all the studied cases have a non-uniform distributed load of thrust and rotational forces applied on the actuator disk, in the present project will be limited to only apply a radial distribution of thrust force since

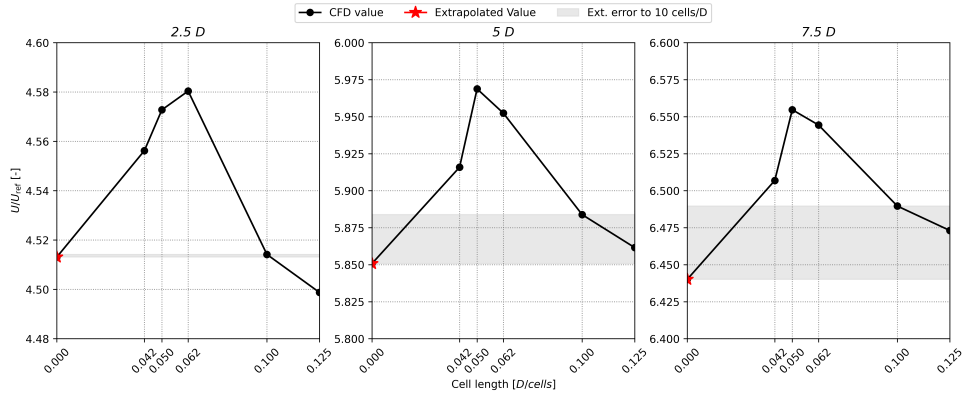

Figure 2.9: Extrapolated solution and error for the first mesh study.

rotational forces are negligible for power deficit measurements (van der Laan, Murcia, et al., 2015). As a consequence, it is expected to get symmetrical wakes since asymmetry is mainly caused by the force rotation.

From (van der Laan, Réthoré, et al., 2015, Figure 5), there can be extracted normalized values of the NREL WT distribution load. To implement it in a generic way in OpenFOAM, an analytical expression for this radial distribution is sought. Previously Réthoré et al. (2014) had proposed the below generic analytical expression for radial thrust force on a WT from the choice of a polynomial order p:

$$\frac{{T_{(r)}}^p}{T} = Cr^{p-1}(r-R) \qquad C = -\frac{p^p}{R^p(p-1)^{p-1}} \tag{2.3}$$

Specifically for NREL distribution, the normalized thrust can based as:

$$\frac{T_{(r)}}{T} = 1.19(0.5{T_{(r)}}^{p=3} + 0.5{T_{(r)}}^{p=9}) \tag{2.4}$$

As eq. (2.4) is normalized to 1 but (van der Laan, Réthoré, et al., 2015, Figure 5) has a peak higher than 1, it has been found that by additionally multiplying by 1.54 times the eq. (2.4), there is a balance between thrust force magnitude and the sum-up of the total distribution in actuator disk. In fig. 2.10 there is a comparison between normalized load shown in (van der Laan, Réthoré, et al., 2015, Figure 5) and the current distribution in the present project. The fitting quality of the load distribution implemented is related to an R-squared coefficient of 0.88. It's noticed a deficit in thrust magnitude that may lead to a not-strong wake as needed when it comes to comparison with measurements. mesh resolution.

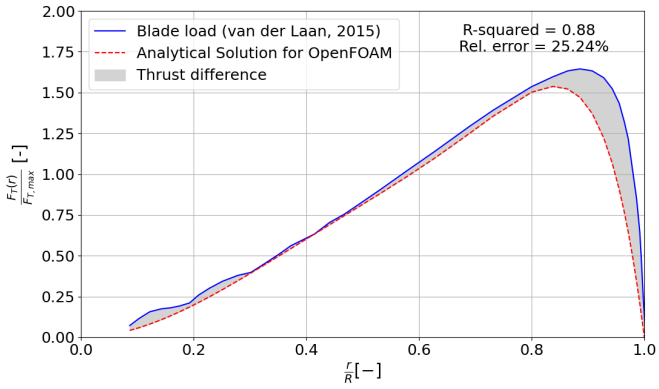

Figure 2.10: Comparison between normalized load distribution used on NREL case study and theoretical.

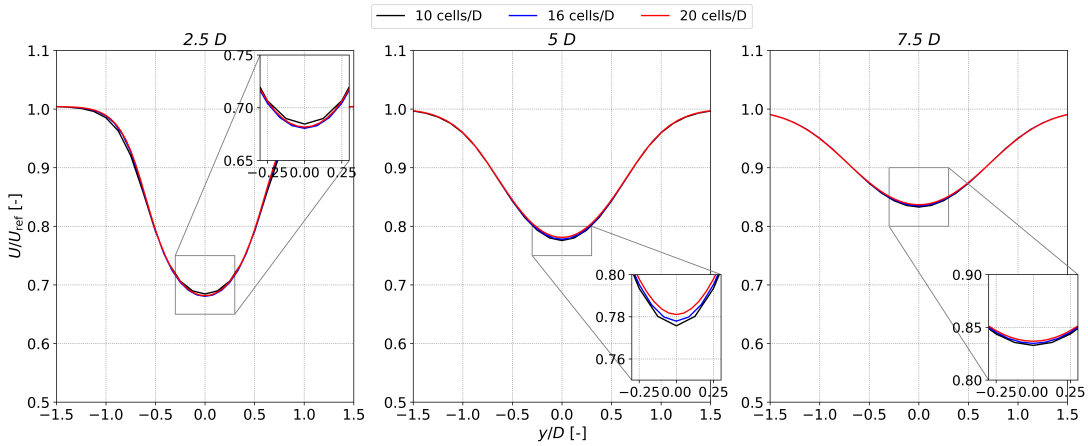

Figure 2.11: Mesh sensitivity study in non-uniformly loaded actuator disk: at downstream distances of x/D: 2.5, 5, and 7.5.

2.5.5 Results of validation

As could be expected, $k-\varepsilon$ had a poor performance whereas $k-\varepsilon-f_P$ has better proximity to van der Laan, Réthoré, et al. (2015). The quality statics for the $k-\varepsilon-f_P$ are summarized in the following table:

2.5.6 Revision between uniform and nonuniform load

When applying the same amount of thrust force magnitude in uniform and non-uniform distributed loaded ADM, the measurement comparison shows that neither average disk nor hub point horizontal velocity values are the same. This is summarized in table 2.6. This confirms the assumption that they do not develop the same vertical profile and may develop a different flow transition before the actuator disk.

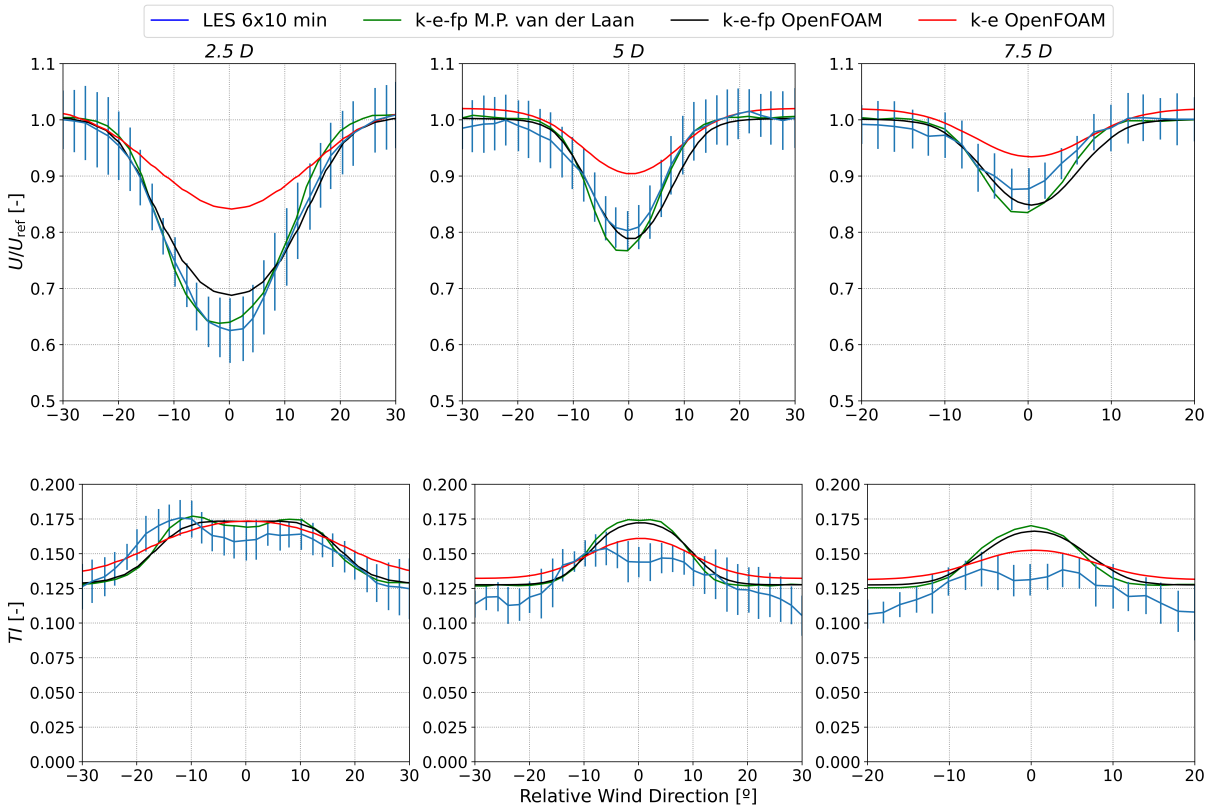

Figure 2.12: Comparison of wakes between models in horizontal velocity wake deficit (top), and turbulent intensity (bottom).

2.5.7 Wake affected turbine

To verify how $k-\varepsilon-f_P$ behaves in a wake environment, it was followed test case 3 from van der Laan et al. (2014), which uses the same NREL turbine but places a second WT 5D downstream and aligned to the first. Here TI_{hub} changes to 8% required an adjustment of z_o to a new value of 0.005m. In this case, both turbines are set to have the same thrust force magnitude with a non-uniform load distribution. Aside from the original set-up, there was also tested a controller method for variable thrust force magnitude. For that, there were performed 5 simulations of a single NREL turbine within $4 \leq U_\infty \leq 8$. The average disk values were tabulated and the algorithm was coded to execute the controller method presented section 1.2.3 from (Navarro et al., 2018). For details, refer to appendix A.4. As appreciated in fig. 2.13, for the prescribed thrust force magnitude there are good matches with LES data, as for the calibrated turbine case, a weaker thrust magnitude has been applied leading to a weaker deficit of velocity in the second rotor, which is understandable since real inflow of the second turbine is slower.

Table 2.5: $k-\varepsilon-f_P$ statistics

		2.5D		5D	
		R^2	Rel. error(%)	R^2	Rel. error(%)
U	LES	0.98	3.49	0.95	1.84
	$k-\varepsilon-f_P$	0.97	3.89	0.95	1.87
TI	LES	0.37	5.76	0.72	7.16
	$k-\varepsilon-f_P$	0.92	1.86	0.99	1.11

Table 2.6: Comparison of uniform and non-uniform cases

	Uniform	Non-uniform	Difference
U_∞ [m/s]	8.00	8.00	-
C_T [-]	0.79	0.79	-
U_d [m/s]	4.89	4.55	0.34
Ux_{hub} [m/s]	6.10	7.46	-1.36

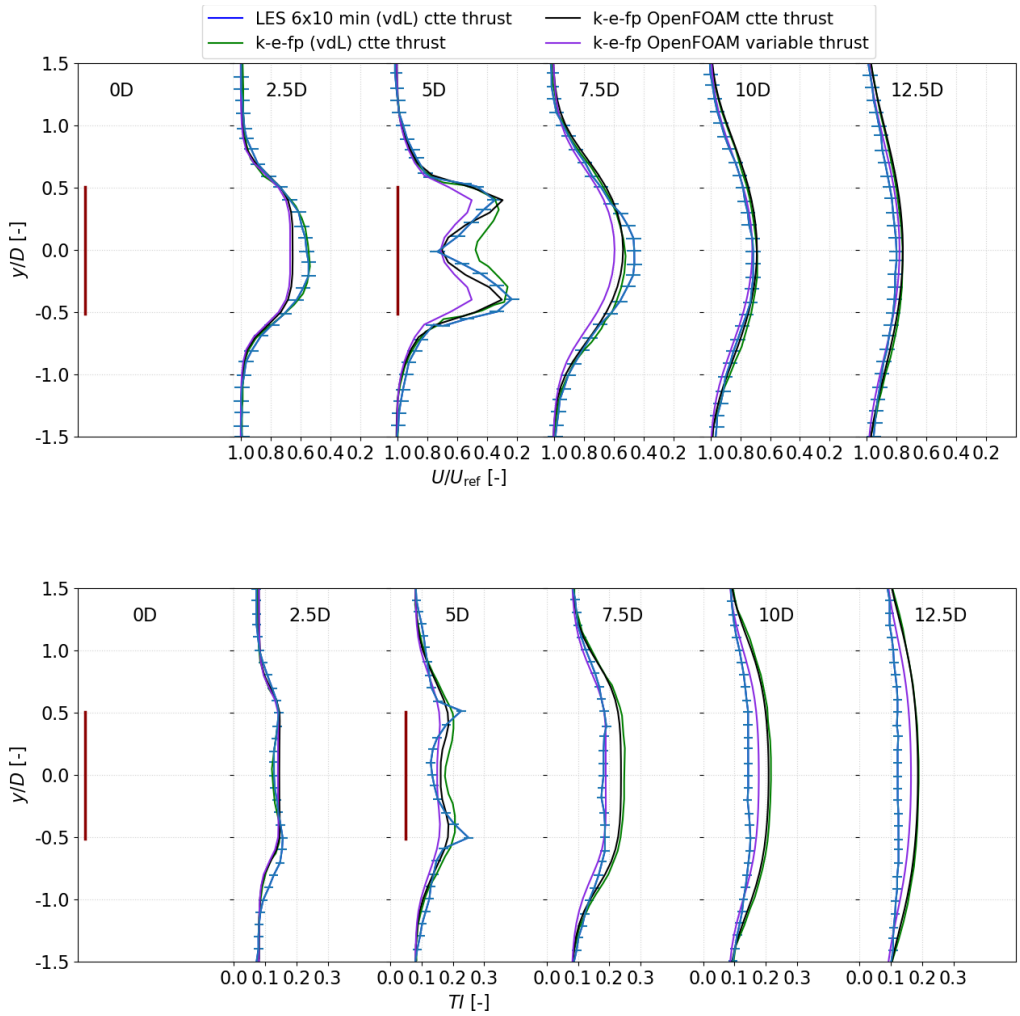

Figure 2.13: Comparison between models of constant thrust force magnitude and variable thrust.

Chapter 3

Pre-processing

To accomplish an evaluation of the performance of the concentrator in Shagaya Renewable Park, the present chapter aims to describe first the case set-up along with the mesh sensitivity study.

3.1 Description of the model

Reference wind speed at hub height U_∞ is set to 8 m/s as a simplification of the wind analysis study shown in appendix A.1. Roughness length used if $z_o = 0.005$ m according to data site in Atlas (2023) for the coordinates of 29º13'32"N 47º02'47"E. From here, a characteristic scale of this case can be defined as $h/z_o = 12/0.005 = 2400$.

The external flow is modeled as neutral homogeneous ASL. The assumption of incompressible and turbulent flow is confirmed by the following verifications in both R_e numbers at the concentrator's top and at the hub point, along with the Mach M number for atmospheric air at 20ºC:

$$R_{e,c} = \frac{U_{c,top}h}{\nu} = 6.3 \times 10^6 \qquad R_{e,turb} = \frac{1}{\kappa^2}\ln\frac{h}{z_0} = 48.64$$
$$M = \frac{U_\infty}{\sqrt{k_{air}R_{air}T}} = 0.0236 \qquad R_{e,hub} = \frac{U_\infty D}{\nu} = 51 \times 10^6$$

Boundary conditions will follow techniques discussed in section 2.5.2 with a logarithmic inlet profile. Moreover, as set already U_∞, z_o, $z_{hub} = H$, the turbulence intensity TI to be read at the hub point in an empty ABL (without turbines) is as a consequence set to

8.1%.

As for the numerical schemes used, the runs are in steady-state RANS using $k - \varepsilon - f_P$ model. The gradients were discretized using Gauss linear scheme with a cell limiter. The convective terms were used Gauss linearUpwindV for velocity and Gauss upwind for turbulence fields accordingly. The laplacian terms with Gauss linear with a limiter. The solvers for the pressure equation chosen is GAMG, and PBiCGStab with DILU conditioner for velocity and turbulent fields. The SIMPLEC algorithm was used along with relaxation factors of 1.0 for pressure, and 0.9 for U, k and ε equations. The convergence is assumed if residuals reach below 10^{-4} and fields sampled by probes in space achieve a steady solution.

3.1.1 Concentrator and tested locations

The wind concentrator body will be a 3D rectangular flat geometry subtracted from the domain. A representative thickness of 0.5 m is used in the design of CAD model. The concentrator will be aligned parallel to the row of turbines and centered on rotor N2 (middle turbine). The distances to be tested are the initial proposal of W'WAVE for 85 m (aprox. 7h). Additional distances are proposed to be included in the analysis: 24 m (2h) and 45 m (approx. 4h).

3.1.2 G97 turbine data and tested actuator disk submodels

Power curve and thrust coefficients for the G97 can be extracted from WTM (n.d.). The G97 will be modeled as ADM and the following cases of implementation shown in table 3.1 will be evaluated:

Table 3.1: Description of implementation cases of actuator disk

Case	ID	U_{ref} [m/s]	C_{Tref} [-]	Thrust mag.	Load dist.	Approach
1	CF	8	0.82	prescribed	uniform	Fixed thrust
2	CA	U_d	2.3	variable	uniform	Calaf
3	CC	U_∞ (read)	$C_{T,\infty}$ (read)	variable	uniform	Controller
4	NC	U_∞ (read)	$C_{T,\infty}$ (read)	variable	NREL	Controller

3.1.3 Parameters for evaluation

For each case of implementation, an equivalent simulation of only ADM (without the concentrator) is launched with the same set-up on the actuator disks as the concentrated versions. Quantification of changes at hub point and other probes, sampling on lines and the average disk values in any field called R, such as: horizontal wind velocity U_x, magnitude of vector velocity U, turbulent kinetic energy k and therefore the turbulent intensity TI, are calculated as:

$$\Delta R_{x_t,method}(\%) = \frac{R_{CFD,conc} - R_{CFD,ADM}}{R_{CFD,ADM}} * 100 \tag{3.1}$$

Where suffixes 'conc' and 'ADM' in eq. (3.1) stand for concentrated and not concentrated accordingly, as 'x_t' refers to the distance of separation between the concentrator and wind turbine and 'method' to the type of ADM implementation applied. If the sign from $R_{CFD,conc} - R_{CFD,ADM}$ is (+), an increase on the field is generated by the presence of the concentrator, whether (-), the opposite.

An analysis on the vertical profiles is practiced by finding the average and dimensionless shear exponent from the power-law velocity profiling in other to capture if the flow carries more shear along the diameter of the rotor at the rotor's plane. This is accomplished by computing the average gradient between each pair of points sampled using their stored values of horizontal wind velocity and heights as shown in eq. (3.2):

$$\frac{U_{n+1}}{U_n} = (\frac{z_{n+1}}{z_n})^{\alpha_n} \rightarrow \overline{\alpha} \ = \frac{\sum(\alpha_n)}{N} \tag{3.2}$$

Finally, the wind power capacity increase are calculated following eq. (1.28).

3.2 Mesh sensitivity study

By combining guidelines for domain sizing for ABL and ADM modeling in van der Laan, Réthoré, et al. (2015) and Franke and Baklanov (2007), the dimensions of the domain are 30 x 38 x 16 D in the directions of streamwise, spanwise and vertical direction as shown in fig. 3.1. The front area of the domain results in a BR at the concentrator placement of 0.17%, at the wind-turbine's row of 0.66%, and if these two were hypothetically combined, BR goes up to 0.84%, a value acceptable from limits set in Franke and Baklanov (2007).

From fig. 3.1 is a sided-top view of the background mesh with an inside view of the location of rotors and concentrator. The background mesh consists of 148 x 375 x 89 hexahedral elements (streamwise, spanwise and vertical direction) generated by using blockMesh tool. To find the suitable mesh for the development of the project, a mesh sensitivity study was conducted by testing three options of hexahedral dominant meshes further elaborated via the snappyHexMesh tool: coarse, medium, and fine. Details of overall cell count and ratios between cases are shown in table 3.2, and details on levels of refinements used are shown in table 3.3 and can be better visualized in fig. 3.2.

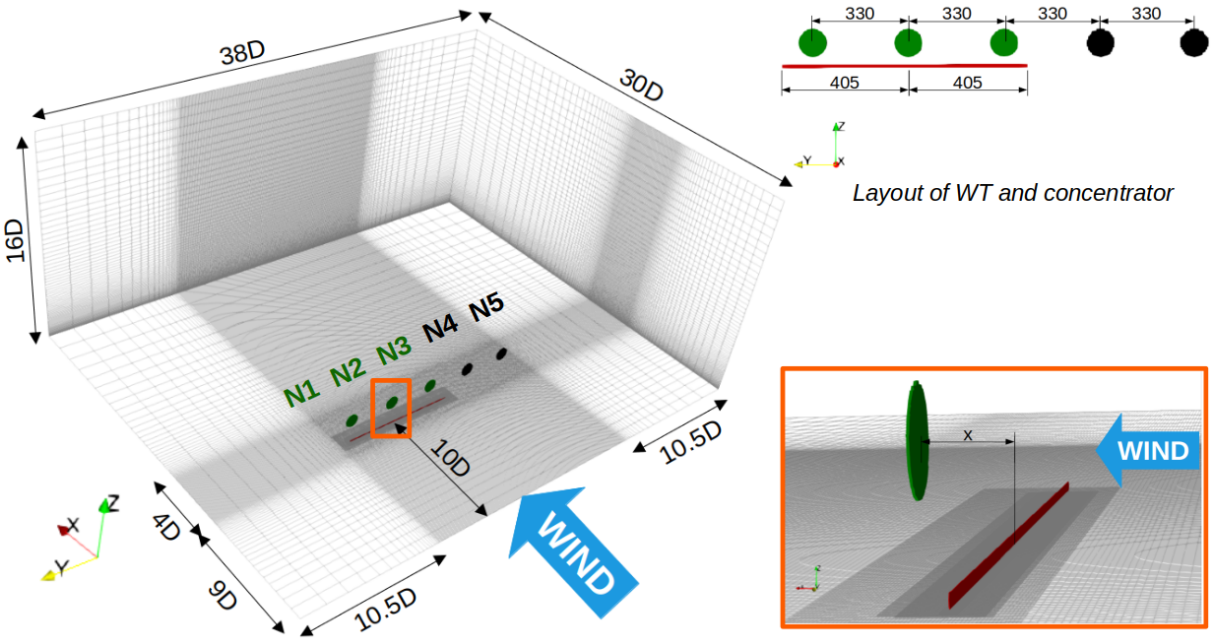

Figure 3.1: Overall top view of the inside of the mesh. Red line: concentrator. Green circles: concentrated sub-system. Black circles: rotors N4 and N5.

Table 3.2: Mesh options summary

Mesh	No. of Cells	Cell size (h)	h_1/h_2
Coarse	9,008,058	0.0048	1.159
Medium	19,688,853	0.0037	1.290
Fine	30,696,200	0.0031	-

3.2.1 Mesh convergence study

The runs on the meshes: coarse, medium, and fine, have in common the ABL set-up, boundary conditions and numerical set-up described in section 3.1 along with CF ADM

Table 3.3: Mesh options and levels of refinement applied

Mesh	$wall_{edges}$	$wall_{surface}$	$nearby_{region}$	$topWake_{region}$	ADM_{region}
Coarse	3	3	1	2	0
Medium	4	3	2	3	0
Fine	3	3	2	2	1

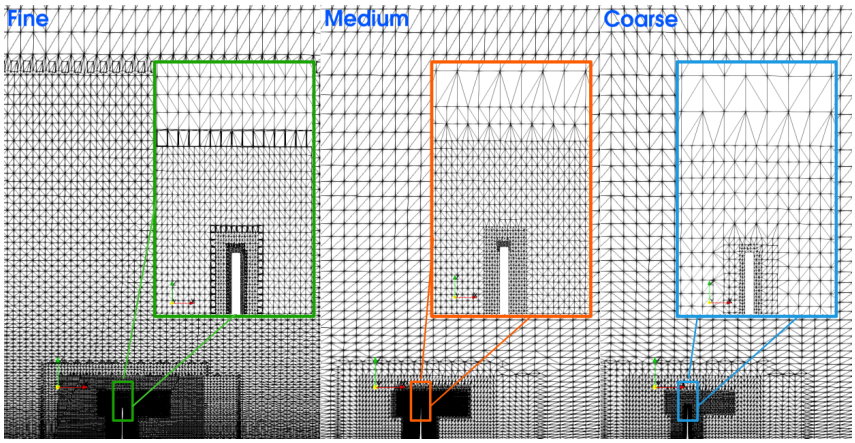

Figure 3.2: A cut-plane view centered at concentrator half of meshes Fine (left), medium (center) and coarse (right).

implementation and an upwind distance of 45 m between rotors and concentrator. In table 3.4 is found a summary of the statistics gathered from the comparison between meshes. It is shown that the extra refinement in the region of the rotor as applied in the fine mesh causes a drift in the values of the velocity and turbulent kinetic energy fields. The fine mesh results in a range of relative errors to the Richardson extrapolated solution within 1.71% and 5.50%, which leads to relative errors in the medium mesh from 2.2% to 7.61%. The highest discretization error in fine mesh is registered at the hub point value of k with a GCI index of 7.27%. The author's choice is to use the fine mesh for the following stages which implied a discretization in the concentrated actuator disk of 40 cells/D whereas for the non-concentrated to 20 cells/D.

New flow pattern

To better understand what is the flow pattern without a concentrator and its modifications due to the presence of the concentrator, in fig. 3.3 is shown the contours of the before and after of fields: velocity, kinetic pressure, and turbulent kinetic energy from rotor N3. Both sets share the same scale in the fields to better appreciate changes in values.

The first column corresponds to horizontal wind velocity Ux, and it is noticed a darkened

Table 3.4: Detailed Mesh Data and Convergence Information

Mesh	$U_{x,hub}$	U_{hub}	k_{hub}	$U_{d,x}$	$U_{avg-disk}$	$k_{avg-disk}$
Coarse (r1)	6.242	6.245	0.754	5.236	5.342	0.840
Medium (r2)	6.249	6.252	0.754	5.244	5.350	0.840
Fine (r3)	6.154	6.158	0.770	5.318	5.427	0.835
Sign of convergences	-	-	-	+	+	+
Order of convergence, p	2	2	2	2	2	2
Extrapolated sol. (e*)	5.881	5.881	0.814	5.533	5.650	0.821
Rel. error (r2/r3)	1.53%	1.53%	2.00%	1.39%	1.42%	0.58%
Extrap. error (e*/r3)	4.64%	4.64%	5.50%	3.88%	3.96%	1.71%
GCI %	5.54%	5.54%	7.27%	5.05%	5.15%	2.11%

region between the center to low-tip level from the rotor which leads to infer a speed-up there. The change in that region in wind speed matches with a drop of kinetic pressure at the same region. Finally, for the third column related to turbulent kinetic energy, the wake of the concentrator introduces an increase of this field at the surface flow downstream, which combined with a deceleration of the flow due to the concentrator wake, may introduce a level of turbulence to the far wake of the wind turbine.

3.2.2 Wall refinement and y+

Since the concentrator has been represented by a 3D geometry subtracted from the domain and, the wall has been modeled as a smooth wall, there is a concern if an acceptable range of y+ could be achieved. There was presented a limitation of generating prescribed inflation layering for a smooth discretization of boundary layer around the wall surfaces when using the meshing tool snappyHexMesh, which is believed the fault relies on the geometry aspect ratio and thickness with the aspect ratio and refinement achieved of the background.

In table 3.5 shows the range of values of y+ gathered in both wall patches: ground and concentrator.

Table 3.5: Summary of y+ values at wall in fine mesh

Patch	Minimum	Maximum	Average
Ground	24.7	20,378.7	3,197.7
Concentrator	1.3	1,283.9	114.3

Close values of y+ = 114.3 mainly cover the concentrator surface at the windward and

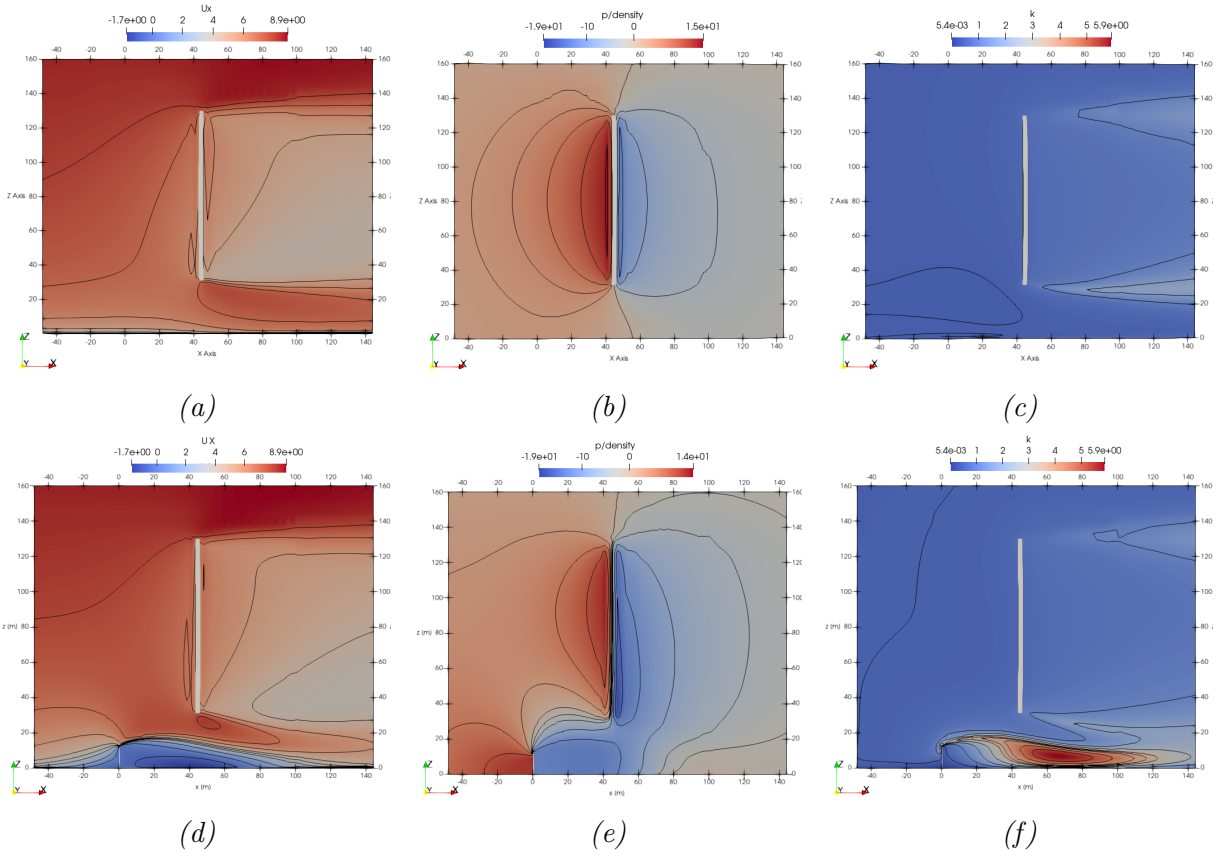

Figure 3.3: Comparison between solutions of only wind turbines models vs. the presence of concentrator using the 'fine mesh. (a-c) Only WT in wind farm, (d-f) wind farm with concentrator.

leeward faces as seen in fig. 3.4 where maximum values up to 1,284 are seen in the edges where is likely difficult to improve the mesh. Values below y+ $<$ 30 are due to the stagnation of flow because of the deceleration induced by the windward face of the concentrator to the flow and the recirculation zone behind the leeward face.

3.2.3 Tables for cases with calibration

As cases described in table 3.1: CA, CC, and NC, require additional input data for computing the variable thrust force magnitude, a total of 5 simulations of single-turbine G97 (isolated) with uniform and non-uniform load distribution where launched. Values of the average disk were gathered and later calculation of induction factor α, Calaf's corrected C_T' were executed, based on $U_{x,avg-disk_{uniform}}$, α and U_∞. As observed in table 3.6, it's noticed that at the average values, the difference between load distribution decreases as wind speed increases, but still, both approaches lead to different values. As for the hub point readings, $U_{x,hub_{uniform}}$ and $U_{x,hub_{NREL}}$, they differ significantly between distributions

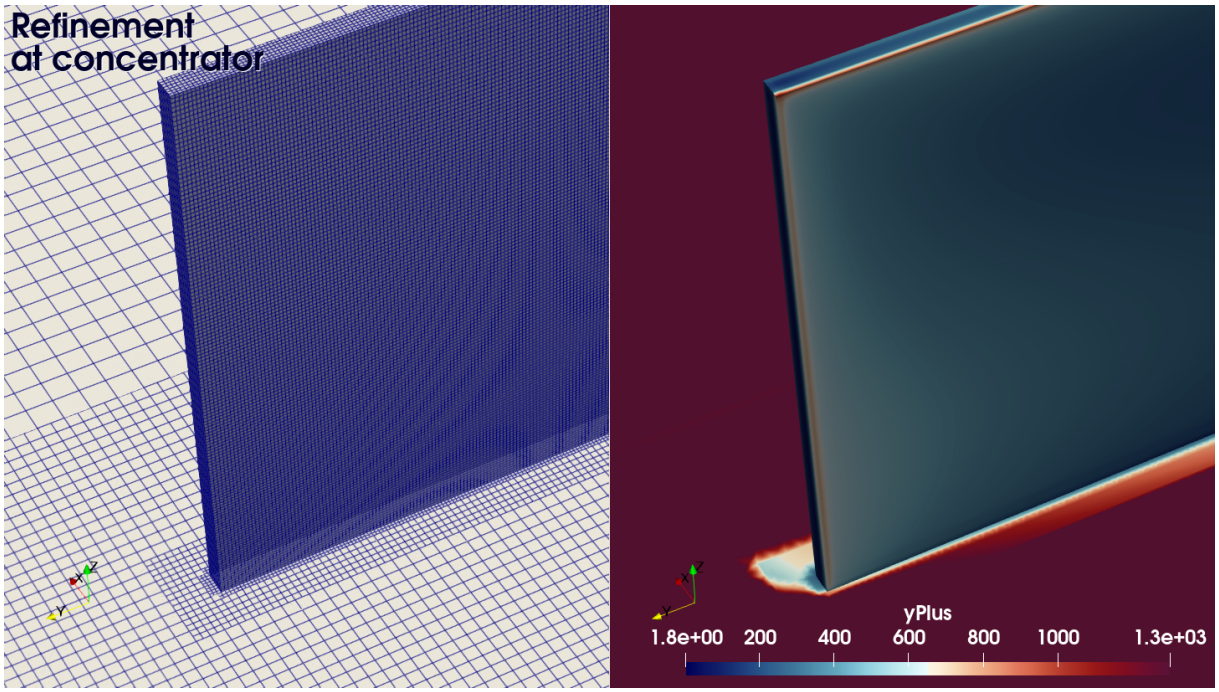

Figure 3.4: Local refinement at concentrator walls (left) and y+ contour map at an extreme side, windward face view (right).

since at methods CF, CA, CC there is thrust applied at the hub point whereas for NC there is not.

Table 3.6: Single-turbine runs of G97 for different wind speeds and different load distributions.

U_∞	**6.000**	**7.000**	**8.000**	**9.000**	**10.000**
C_P	0.450	0.460	0.470	0.460	0.410
C_T	0.830	0.830	0.820	0.760	0.620
$U_{x,avg-disk_{uniform}}$	3.547	4.138	4.782	5.723	7.175
α	0.409	0.409	0.402	0.364	0.283
C'_T	2.375	2.375	2.295	1.880	1.204
$U_{x,avg-disk_{NREL}}$	3.244	3.785	4.392	5.368	6.948
$Diff_{reltoNRELdist.}$	9.33%	9.33%	8.88%	6.61%	3.27%
$U_{x,hub_{uniform}}$	3.642	4.249	4.907	5.850	7.282
$U_{x,hub_{NREL}}$	5.869	6.847	7.827	8.817	9.834
$Diff_{reltoNRELdist.}$	37.94%	37.94%	37.31%	33.65%	25.95%

For the solution of CA subcases of upwind distance: $2h, 4h, 7h$, the value of $C'_T = 2.30$ from table 3.6 for $U_\infty = 8.0$ m/s will be used.

Chapter 4

Results and discussion

4.1 Concentrated turbines

As defined in section 3.1.3, all the values gathered from the simulations of non-concentrated wind farm system are used as reference values for comparison and computation of relative values such as ratios of net wind speed increase, of net turbulence intensity changes and finally, of wind power capacity increase.

4.1.1 Statistical values

Although the absence of field measurements to perform a validation of the models described in table 3.1, a qualitative evaluation can be performed by looking if trends and promising values of wind speed increase appear. Some common patterns can be observed from the hub point result in fig. 4.1 and disk-average values fig. 4.2 results.

From the hub results:

For all the cases stated in table 3.1, regardless of the implementation, there can be observed in fig. 4.1 an increase in the horizontal wind velocity at hub points along with a decrease in TI levels. It happens also, that the centered turbine (N2) has these benefits at a higher level than the wind turbines at the sides (N1 and N3).
Solutions from the centered and side turbines from cases CA, CC, NC seem to be bounded within a range. The CA method has maximum values at 4h for all three turbines, being the highest of 3.24% on N2, where the lowest values are registered at 7h for the side turbines and 2h for the N2, within a difference of 0.29% between maximum and minimum

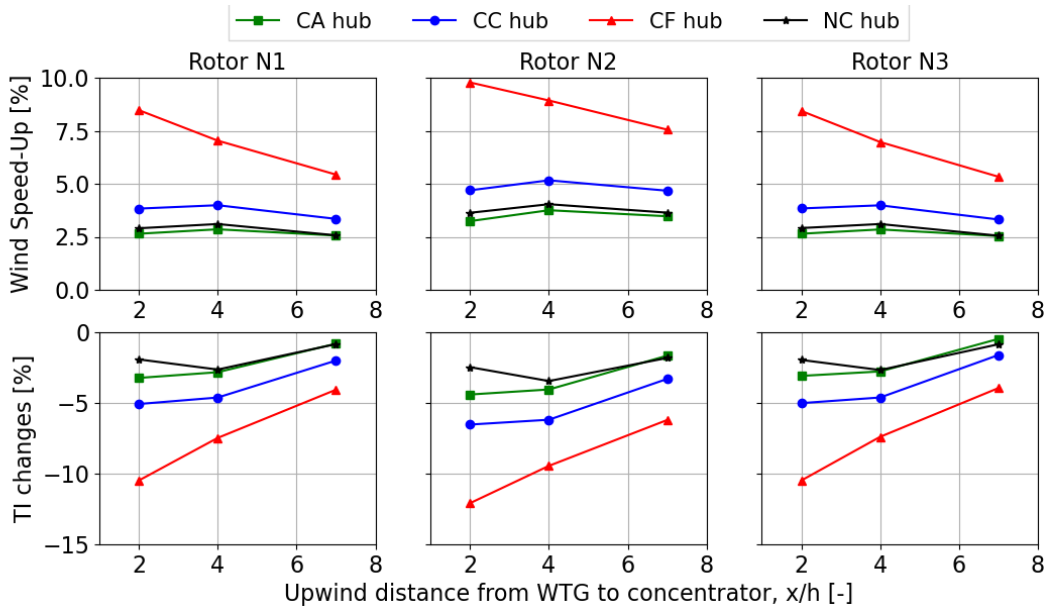

Figure 4.1: Speed-up of horizontal wind velocity (top) and changes in TI (bottom) at hub point.

values. As per the CC case, the highest values are at 4h for all turbines being the highest value of 4.67% for N2, the lowest at 7h for the side turbines with 2h for N2, and a difference between maximum and minimum values of 0.6%. The other case of similar output to the previous ones is NC, here 4h provides the highest increase for the three turbines with a value of 3.63% of wind speed increase at N2, and one more time, 7h shows the minimum value for the side-turbines and 2h for the center turbine, leading a difference of 0.5%. On the other side, the CF case shows an outstanding wind speed increase way higher than the previous cases and a different pattern from the others, whereas closer to the turbines, the greater the wind speed increase and so proportionally, the decrease in TI.

Both cases, CA and CC, which have in common the uniform-loaded distribution, share the trend of decreasing TI as closer the concentrator is to the turbines. This pattern is not found at NC, where 4h has the highest decrease on each turbine.

The present approach of the physics by solving steady RANS with an isotropic model does not resolve the temporal turbulent structures that develop in atmospheric flows and the possible asymmetry that could be developed also in the wakes, based on this clarification, the present results of a decrease in TI values can be considered at least, as indicators that the concentrator does not introduce additional turbulence intensity to the rotor region in the current configurations and a safety margin from the last happening goes in accordance of the TI decreasing read.

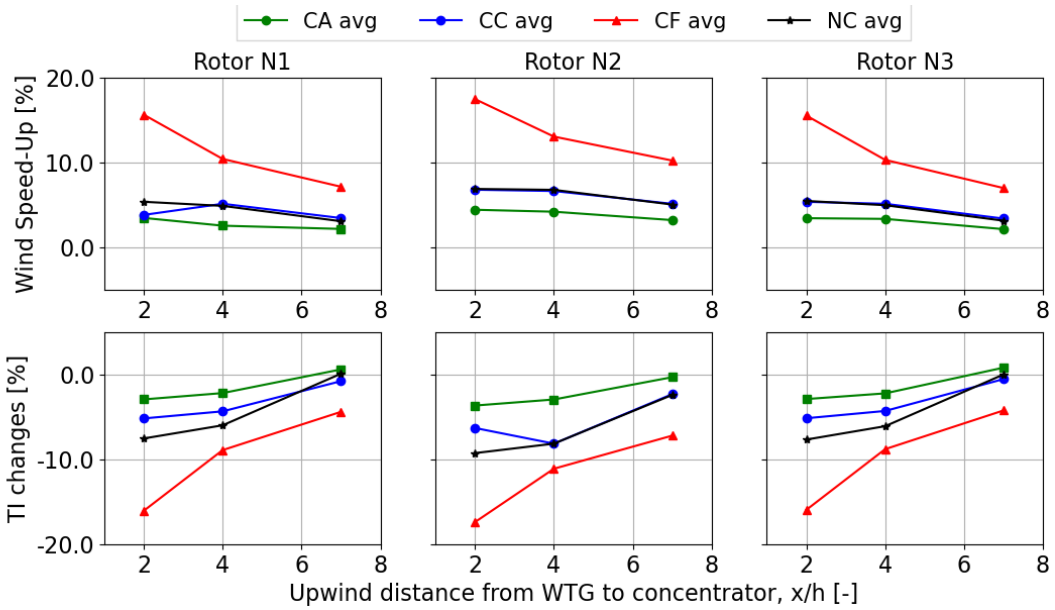

Figure 4.2: Speed-up of horizontal wind velocity (top) and changes in TI (bottom) at disk-average.

From the average-disk results

The speed-up effect of the concentrator is known to affect more in the lower region of the rotor than at the hub or top, and that's seen at fig. 4.2 where higher changes are gathered if compared to fig. 4.1.

For all the cases and wind turbines, higher values of wind speed increase are found at 2h and the lowest at 7h. Cases CC and NC have almost the same solution for wind speed, both follow a controller method, but, CC shows to have a higher TI decrease at N2 for a 4h distance. As for the CA implementation, both the speed-up effect and decay in TI are the lowest outputs compared to the rest which is something similar seen at hub points. One more time, CF method shows up with the highest wind-speed increase and decrease in TI as the concentrator gets closer to the turbines.

A possible explanation for the higher changes in N2, which is the turbine in the center, concerning N1 and N3 which are the side turbines, is that for N2 the relation between diameter and concentrator's length is approx. 8.35D, whereas for N1 and N3, the remained section of the concentrator that extends after the end of each rotor area of N1 and N3 is 0.33%D in addition, so it could be stated that for these side-turbines, the corresponding relation of concentrator's length between turbine diameter and the portion of concentrator that exceeds the rotor, is (0.33D + 1D +0.33D) = 1.66D for each. Recalling the literature from (Tobin & Chamorro, 2017) and (Liu & Stevens, 2021), the concentrator's length for

the single turbine they tested are 2D to 5D of the length of the concentrator. The range of inflow aligned to N2 is forced to pass over the concentrator, whereas, for the side turbines, part of the flow passes over the concentrator or laterally surrounds this at the leading edge. This implies that the aspect ratio of concentrator dimensions and turbine diameter is key to designing the concentrator system.

At this stage, possible benefits in energy production can range between the studied distances of 2h and 4h.

Vertical profile changes at rotor plane:

Another point to evaluate is whether the concentrator recreates a more or less shear inflow to the rotor. Comparison in rotor N2 for the cases with a 4h distance is made by taking vertical sampling along the rotor's center line passing through the hub point. A before and after wind profile can be observed in fig. 4.3.

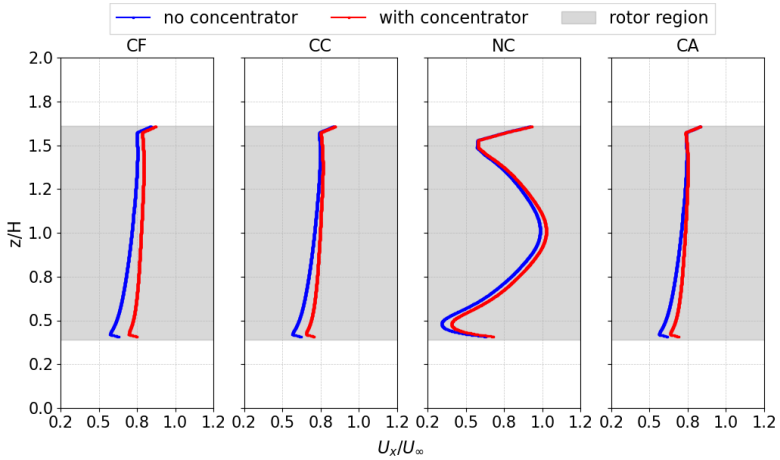

Figure 4.3: Comparison of vertical profiles of horizontal wind velocity before and after the presence of concentrator taken at rotor plane of turbine N2.

It's common in the sub-figures to see an acceleration in the vertical profiles from the concentrated systems compared to the version without the concentrator. The CF case shows a greater difference between with and without concentrator along the whole vertical profile, with a 9.83% of overall increase in wind speed distribution as seen in table 4.1, whereas for the rest, the changes are limited mainly from the hub point to the low tip accompanied by an increase between 4.58% to 6.24%. An interesting output in fig. 4.3 is the overall difference in the wind profile based on the choice of thrust load distribution which is seen in the unique "$\sum$" shape in NC.

Table 4.1: Average values gathered from comparison of vertical profiles

Case	Speed-Up	Shear no-Conc	Shear w/Conc
CC	6.24%	0.2867	0.1993
CF	9.83%	0.2819	0.1777
NC	5.79%	0.3692	0.3042
CA	4.58%	0.2893	0.2097

A lesser shear flow or more likely, a 'vertical uniform flow' would enhance the wind turbine blades' lifetime by reducing dynamic loads and fatigue. A before and after of the characteristic shear exponent value at rotor can be reviewed in table 4.1. In each case, the concentrator lowers the shear exponent of the flow profile. The highest drop in shear corresponds to CF case, and the lowest correction to NC case. Cases CA and CC develop almost the same performance of wind flows.

Recalling the literature, (Simisiroglou et al., 2017) states that non-uniform thrust distribution is a better representation of the rotor loading than uniform distribution. Therefore, NC case providing a lesser value of shear exponent represents an improvement in site conditions.

4.1.2 Overall changes in regions

An additional way to visualize changes is by reading heat maps of the differences in velocity and turbulence intensity fields. Contour plots are gathered for the N2 turbine in the case of 4h distance.

As per the changes in velocity, fig. 4.4 shows for each case the flow of different shapes. The CA outputs a thinner vertical region where wind speed is increased, followed by CC where this extension widens up to finally a broader region in CF where also darkened coloring is seen at the top tip. As for NC, a speed-up at the hub height level goes after 2D downstream. In common for all the profiles, a speed up above the top tip of the rotor is observed along with a higher wind speed deficit at the turbine's wake.

From fig. 4.5 it's observed that at the same region of wind-speed-up effects is where the decay in turbulence intensity happens. The highest drop and widest region are related to CF, followed by CC and NC, and last the CA case where changes are more conservative. In this case, turbulence intensity drops at the nearby region of the rotor but introduces turbulence in the wake of the turbine.

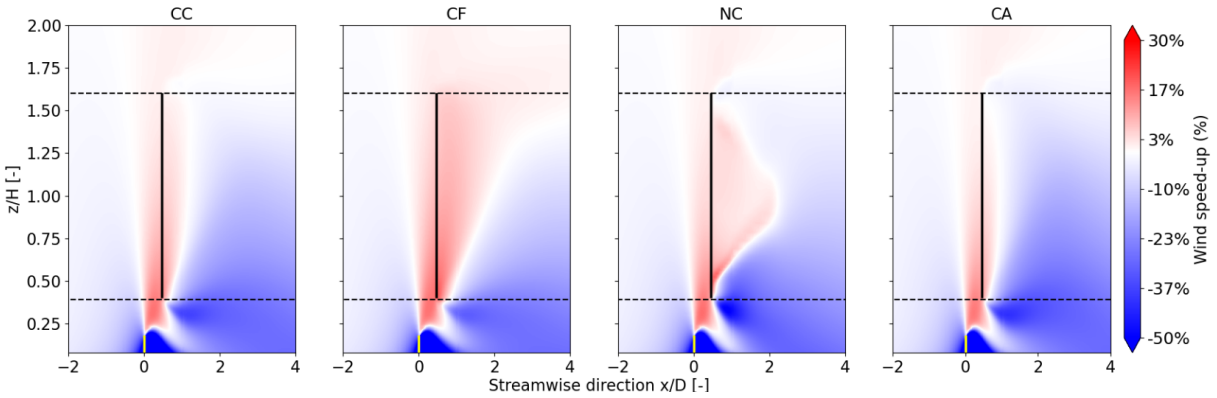

Figure 4.4: Contour of wind speed changes in the close area of wind turbine N2 by each ADM method with a 4h distance. Dashed lines delimit the rotor region. Solid line: rotor's location. Dashed lines: lower and upper tips of the rotor.

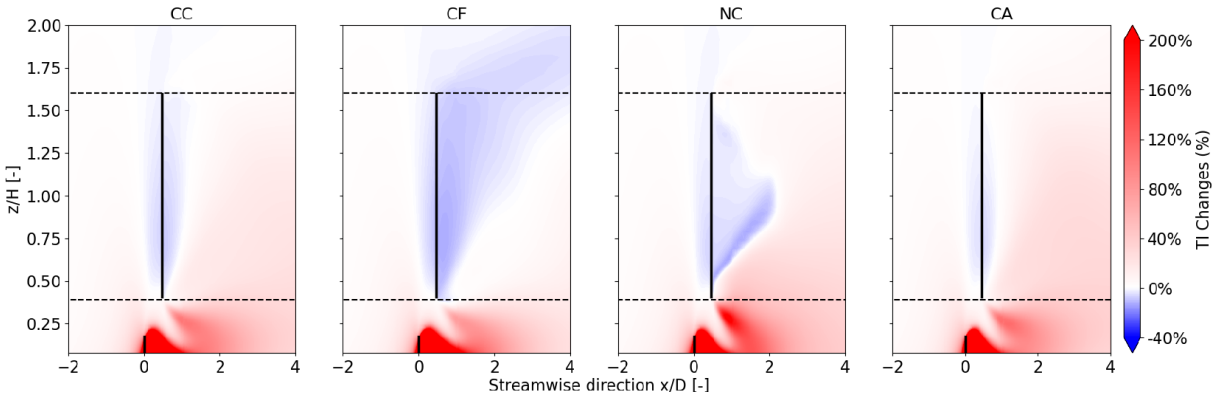

Figure 4.5: Contour of turbulence intensity changes in the close area of wind turbine N2 by each ADM method with a 4h distance. Dashed lines delimit the rotor region.Solid line: rotor's location. Dashed lines: lower and upper tips of the rotor.

An additional contour of difference from before and after as fig. 4.6 which is located at a center rotor plane can provide information if there are imbalances in the nearby regions of the rotors.

Since no increase of TI levels is observed in the measurements of each *ADM* at hub points and average disk values, additional observation in figs. 4.1 and 4.2 and in figs. 4.5 and 4.6 indicates that the area of rotor's swept area has no increase either in TI, then can be stated that the wind turbine would remain operative in the class condition for which it was designed if the concentrator is installed.

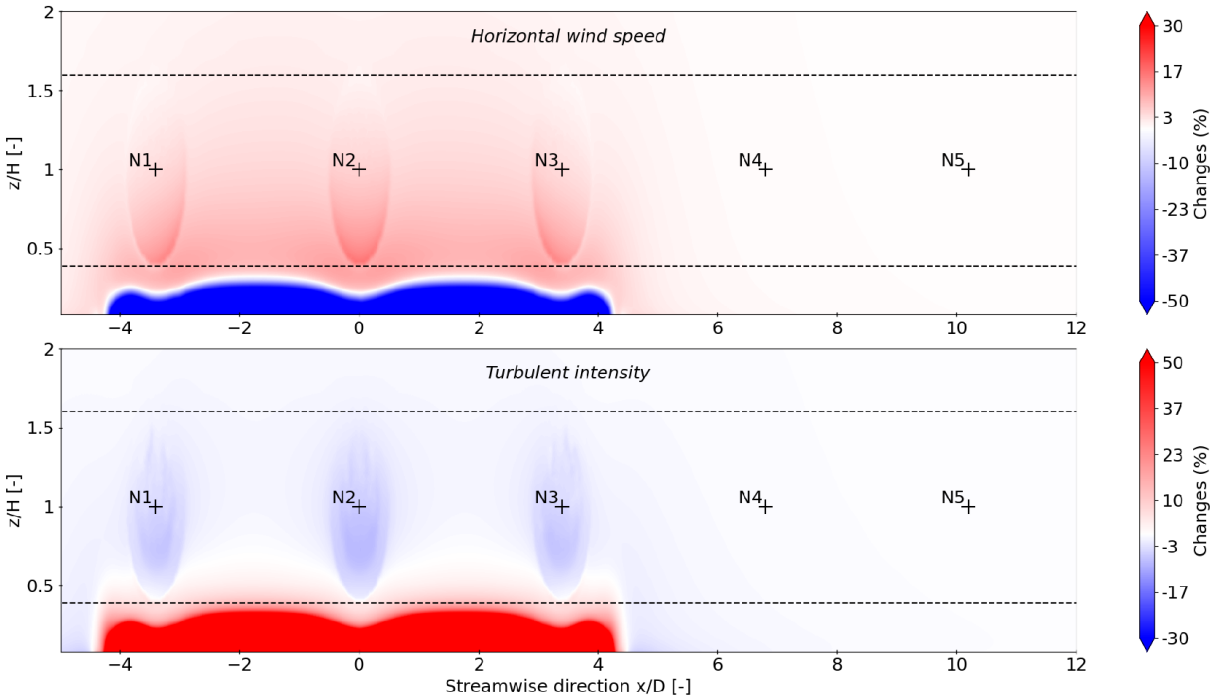

Figure 4.6: Contour of changes in wind velocity and turbulence intensity changes at the rotor plane of rotors for case CC at 4h distance. Cross markers: wind turbine hub points. Dashed lines: lower and upper tips of the rotor.

4.2 Net power capacity increase

4.2.1 Theoretical solution

Recalling the linear theory of Tobin et al. (2017) shown in eq. (1.29), if applied to the current characteristic of the concentrator: solid surface $\eta = 0 \rightarrow \alpha_c = 1.2$, $h/z_{hub} = 0.15$, $\beta \approx 0.048$, the estimation in wind power capacity increase concludes in $\frac{\Delta P}{P_0} = 0.132 \rightarrow 13.2\%$

However, the experiments from Tobin et al. (2017) only stood for a 5h distance, and eq. (1.29) is not correlated to the upwind distance x_t/h, and only accounts for changes at hub point. Despite this, this theoretical value will used as a reference to review the final output in power increase that the cases obtained.

4.2.2 Comparison between cases

From the calculation of net wind power increase and the ratio between older power value of the system using eq. (1.28), fig. 4.7 exhibits in (%) the final performance of each case. As it can be seen in table 4.2, based on hub readings all the cases underestimate $\frac{\Delta P}{P_0}$

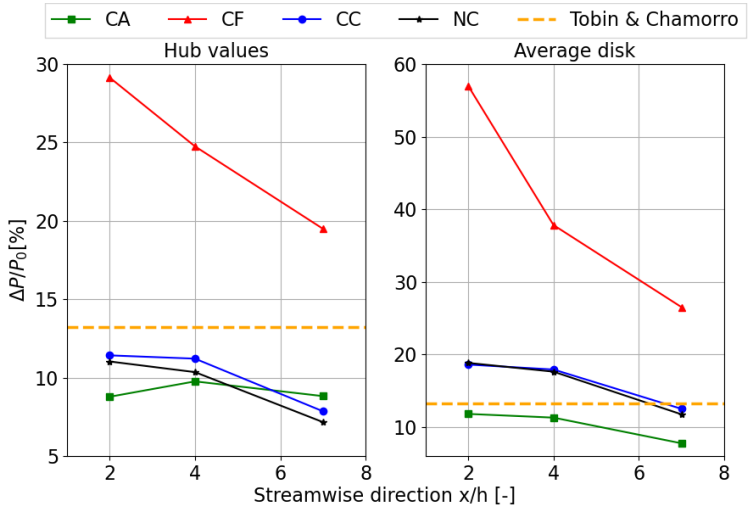

Figure 4.7: Ratio of wind power increase of the concentrated wind turbines system if computed from hub values (left) and if computed from disk-average values (right).

except for CF case which tends to double and even quadruple the theoretical value. As expected, as average disk values in fig. 4.2 were higher than fig. 4.1, the net wind power would be, and, it is observed as an overestimation found for all the cases except for CA. The benefits gathered at the lower part are not considered in the traditional expression of the power output of eq. (1.24).

Table 4.2: Relative error between $\frac{\Delta P}{P_0}$ and theoretical solution.

	Average-disk				**Hub**			
x/h	**CF**	**CC**	**NC**	**CA**	**CF**	**CC**	**NC**	**CA**
2	331.89%	40.92%	42.69%	-10.63%	120.76%	-13.52%	-16.47%	-33.52%
4	186.55%	35.75%	33.50%	-14.47%	87.52%	-15.06%	-21.59%	-26.04%
7	100.83%	-5.29%	-11.04%	-41.29%	47.65%	-40.55%	-45.76%	-33.19%

Solutions from CC and NC cases show a similarity in curve pattern and similarity in values with differences within 2% and 6%, reminding what has been observed already in section 1.2.2, where literature shows that both methods are effective in measuring ratios of changes, regardless the real absolute values of measurements. While case CC and NC could be thought to be the closest to reality responses of the turbines to disturbed inflow since they try to adjust themselves following the manufacturer's power curve, case CF is a prescribed operating condition that does not adjust to the previous documentation and its in-field implementation would require special set-up of the wind turbine's control.

4.2.3 Locations and gains

If the theoretical value from Tobin et al. (2017) were confirmed true, results from the hub in table 4.2 defines 2h upwind distance as the optimal distance by slight difference with 4h that almost presents the same output as 2h. However, 7h being the farthest position leads to the insight that growing the distance after 4h does not improve performance. The final choice of either 2h and 4h for the present project will have to be reviewed on the availability for the installation of the terrain at those given distances (does not interfere with roads, access passages, or with protected areas).

Since the highest improved region is the lower region of the rotor as observed in fig. 4.4 and leads to a higher enhancement in disk-average values than hub results, the following research finds it convenient to determine a wind power increase by weighting equally both curves from fig. 4.7 into a new one and grab overall estimated capacity gains from the new curves shown below:

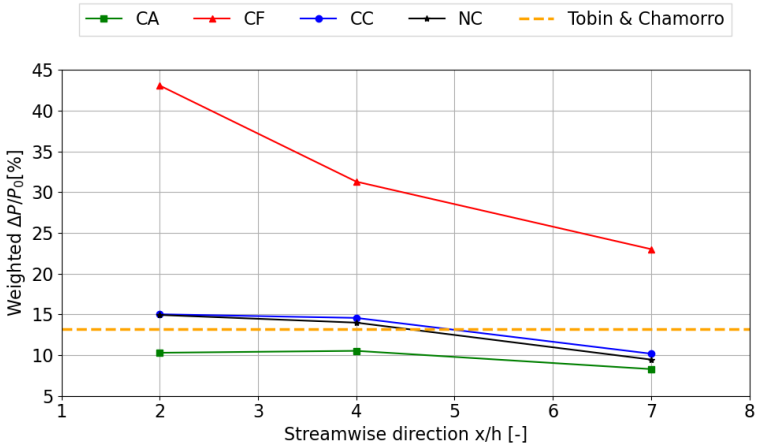

Figure 4.8: Weighted solution of wind power increase based on hub and disk-average values.

Here the outputs of CC and NC are closer to the theoretical solution and final gains on the concentrator implementation in site would be expected to be within 8 to 15% discarding the outstanding gains displayed on CF case.

4.2.4 Changes in non-concentrated turbines: N4 and N5

Turbines N4 and N5 were modeled by the CF method (prescribed thrust magnitude) with the assumption of not receiving perturbed wind. Hub values were monitored and the following changes in wind power based on eq. (1.28) are found in fig. 4.9 for each case:

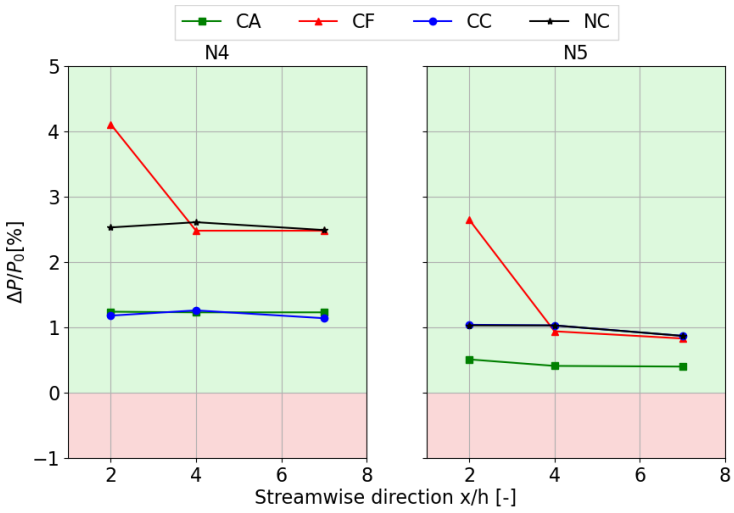

Figure 4.9: Wind power increase in non-concentrated turbines: N4 and N5.

A pattern is slightly maintained between methods for the turbine N4 as seen in fig. 4.9. Here, the wind velocity fields were speeded up, so it's seen a positive $\frac{\Delta P}{P_0}$ in all the methods and distances. The maximum value gathered is from CF at 2h with 4.11% followed by 2.61% resulting in NC at 4h, where for 7h CF and NC provide almost the same value around 2.47 +/- 0.1 %. The rest of the methods, CC and CA, provide a bounded solution for all the distances within 1.14 % upto 1.24 %.

A similar solution is found for turbine N5 where all distances and methods provide positive results. The solutions between CC, CA, and NC give a bounded $\frac{\Delta P}{P_0}$ within 0.4 % to 1.04 %, except for CF which indicates a higher $\frac{\Delta P}{P_0}$ of 2.65 % at 2h.

4.2.5 Overall net power increase in the concentrated wind farm

Finally, to make a final choice on the upwind distance, fig. 4.10 can provide insights of overall wind farm performance per case and distance tested.

It can be once observed in fig. 4.10 that differences between 2h and 4h for methods CA, CC, and NC are small, but still, 2h provides a higher wind power increase in the predictions of CC and NC of 17.22% to 18.49%, respectively. Whereas the solution of CA leads to a slight difference of 0.13% between 2h and 4h, being higher than the 4h solution with 12.16 %. It's also observed that with further spacing from 4h, the rate of increase of wind speed diminishes in a different slope than the section 2h-4h, so 4h can be assumed to be a limit of efficient upwind distance for a concentrator.

To summarize, the methods to handle a wake-affected turbine obtained from the literature

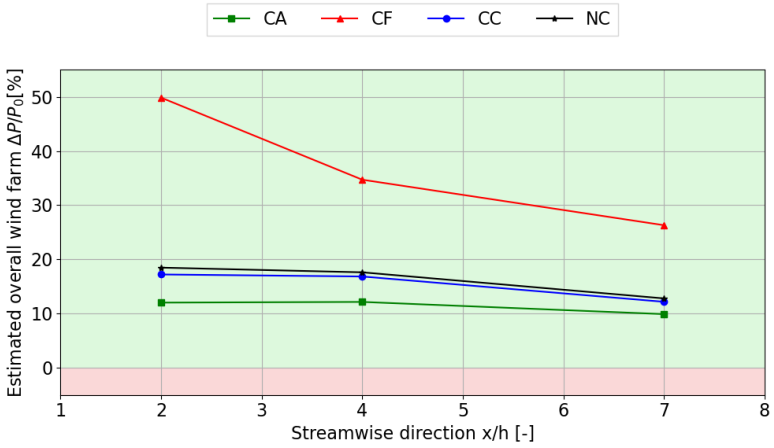

Figure 4.10: Overall wind power increase in Shagaya's wind farm.

review (CA, CC, NC) provide a bounded range of gains in $\frac{\Delta P}{P_0}$ for 2h [12.03, 18.49]%, 4h [12.16, 17.62]% and 7h [9.91, 12.81]%. The method CF once again predicts increments higher than CA, CC, and NC, which introduces an insight into a different way of handling turbine modeling and operation in the presence of a concentrator.

4.3 Signs of a new operative condition

Following insights collected from figs. 4.1, 4.2, 4.8 and 4.10, a brief review of the relationship between $\frac{\Delta P}{P_0}$ increase and thrust magnitude changes will be reviewed.

4.3.1 Relationship between thrust and net power increase

In fig. 4.11 a dual plot is presented to relate a pattern of power increase levels to thrust magnitude changes for each method, and each distance.

It is observed from fig. 4.11 that if the thrust magnitude is kept constant, the maximum wind power increase is obtained. As the thrust magnitude changes increases, meaning that the turbine exerts a higher thrust magnitude with the concentrator than without it, the lesser the wind power increases with the presence of the concentrator.

4.3.2 Theoretical approach to the new condition

The inquiry that arises now if it would be possible to keep constant the magnitude of thrust force despite the presence of a concentrator, while the wind turbine is operating in steady conditions when a few diameters upstream is read some U_∞ value. This looks

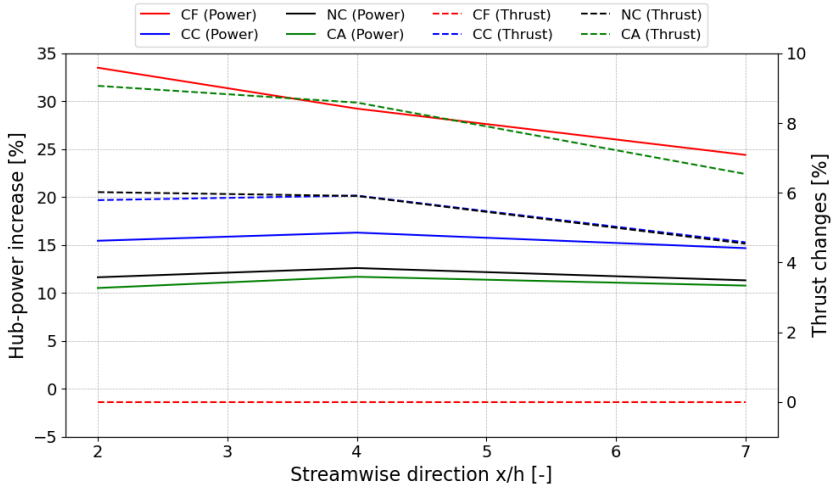

Figure 4.11: Comparison of wind power increase at hub point of N2 against changes in the thrust magnitude between solutions with and without concentrator.

forward to obtaining the gains in wind speed observed in fig. 4.7 and in table 4.2. Bringing back equation eq. (1.23):

$$T = 0.5\rho A U_\infty^2 C_T \rightarrow T = cU^2 C_T$$

If wind speed is increased (U_1 increases to U_2), but thrust magnitude T shall be kept constant, then $C_{T,1}$ must be adjusted for this purpose to a new value $C_{T,2}$:

$$\begin{aligned} cU_1{}^2 C_{T,1} &= cU_2{}^2 C_{T,2} \\ C_{T,2} &= C_{T,1}\left(\frac{U_1^2}{(U_1+\Delta U)^2}\right) \end{aligned} \tag{4.1}$$

This leads to a forced reduction of C_T outside the manufacturer's power curve for a given $U_1 = U_\infty$ that could be performed manually by the operational staff of the wind farm by setting the blades into a new pitch angle. A new open point that comes up from this hypothesis if this new blade set-up of pitch angle position will have a compatible cross-over lifting surface of the airfoil profile of the blade that allows the rotation of the rotor and so the production of energy. To find answers to the previous statement, BEM theory should be reviewed, and relationships of $C_{T,2}$, ΔU and pitch angle from the blade's airfoil data shall be derived but this ends to be outside the scope of the current project.

Conclusions

In this research, a model procedure for performing steady-state RANS was conducted to predict the optimal allocation of a concentrator structure from a wind turbine to optimize the wind power production of a single-row wind farm in flat terrain. The model foundation comes from previous simulations of validation by similarities in neutral atmospheric flows over buildings and on flat terrain single wind turbine cases in the surface layer, which if combined are trusted to recreate a field-case model of concentrated wind flow in wind farms to compensate the lack of field measurements to validate the model.

The literature reviewed in the research additionally lacks of detailed comparison between current CFD techniques of actuator disk implementations, which was thought to have a direct impact on how the inflow transitions from undisturbed flow to the rotor region. This research addressed a comparison to determine if the technique of actuator disk implementation could have a significant role in the solutions of the use of concentrators in wind farms.

Three potential upwind distances from the wind turbines were studied: 2h, 4h, and 7h. To all of them, four different actuator disk implementations for handling perturbed inflows, identified as cases: CA, CC, NC, and CF, were tested (for a detailed description please refer to table 3.1).

Based on qualitative and quantitative analysis of the cases stated of actuator disk cases and the distances tested, the simulations revealed an enhancement in the inflow horizontal velocity due to the presence of the concentrator. Additionally, as shorter the distance from concentrator to the wind turbines, the higher the effect of wind speed-up. A slight difference between outputs of 2h and 4h distances is found so the final decision of the concentrator's placement should rely on the availability of terrain for the facility.

The comparison analysis of cases on the concentrated system showed similar outputs for CC and NC which were supposed to create a self-adjusted wind turbine following the

manufacturer's performance curve with different load distributions (uniform and NREL distribution accordingly). The results shown are defined as wind power capacity increment since production requires corrections with C_P coefficient. These cases resulted in increments of wind power capacity on the system of 3 concentrated turbines, based on hub values ranging from 12% to the shortest distance and 8% for the further distance. CA case follows a different pattern in the power increment at hub values giving the peak of power increment of 10% at 4h distance, but with a similar trend to CC and NC on average values. Finally, the CF case which is a prescribed condition of constant thrust magnitude, shows the highest power increase within all four cases showing a peak in increment of power of 29% at 2h.

Although the existing literature defines the power capacity only by hub values of horizontal wind velocity, the results indicate a higher level of enhancement on average disk values than at hub point values, something that catches the interest to reconsider the power capacity calculation and aims to take in account a weighted contribution of the high speed-up effect found in the lower region of the rotors. To address the definition of the new wind power calculation, the author proposed to weigh equally the power at the hub with the power calculated with disk-average values. The outcomes show for cases CC and NC an increment of power estimated to 10% to 15% from the farthest position to the closest to the turbines tested. CA method is bounded from 8 % to 10.5% and CF ranges from 23% to 43% from the farthest position to the closest.

Non-concentrated turbines N4 and N5 settled registered changes in the velocity field leading to changes in their wind power capacity of each. Positive values but close to zero of $\frac{\Delta P}{P_0}$ resulted in the 4 methods for the 3 distances tested, leading to an insight that these neighbor turbines may be not negatively affected by the presence of the concentrator.

As per the author's point of view, the suitable ways to handle the CFD study case of the wake-affected turbine, as it can be the wind turbine in the presence of a concentrator is by order of preference: the customized to a known load distribution of the 'NC' type of implementation, if not known the load distribution, then go up to CC implementation and last, CA implementation because it fixes for all wind turbines the C_T which could carry numerical errors associated to 1D theory. On the other hand, CF is not completely discarded since results illustrate the higher values of enhancement on all the positions and raise a new hypothesis on higher wind speed-up achievements if it is found a way to keep

thrust force magnitude constant. This last is left as an open point that requires further study which is outside the scope of the current research.

The results of this research lead to a better understanding of how the concentrator modifies the inflow of the wind turbine and provide an orientation on how to evaluate the power capacity enhancement in any other study case within the approach of steady-state RANS and neutral ABL. This is convenient for the industry or any field of research where computing resources are limited to perform a higher fidelity simulation such as LES.

Although a prediction of wind power capacity increment has been elaborated, it's mandatory to recall the limitation of the present research:

- The conditions of ABL had been addressed solely as neutral shear-driven flow.
- The simulations were performed as steady-state RANS so there was no output information on the eddies sizes that the concentrator could generate.
- There is no field experiment documented for validation to clarify if the current turbulence model requires calibration or not.
- Information of C_T values for the G97 was taken from an e-commerce website of wind turbines and not directly read from the manufacturer's manual. Information on the blade airfoil profile is also not known.
- The availability of computational resources could not let to extend the present study to unsteady RANS.
- Neither nacelle nor tower had been modeled.

To conclude, a positive impact of wind concentrated system (N1, N2, and N3) and in the non-concentrated turbines (N4 and N5) has been determined as 2h upwind distance and a prediction of wind power increase of within 12.03% to 18.49% for the wind farm of Shagaya Renewable Park. The objectives are considered to have been covered and future work will be recommended.

Future work

Based on the research results and the limitations found, the author recommends the following topics for future research to extend the present analysis on single-row wind

farms in flat terrain:

- Effects on the wakes in different thermal stratification of ABL. It can be assumed that a stable ABL could deliver a more turbulent wake of the concentrator whereas in unstable conditions, the wake may be diffused sooner and might lower the speed-up effect.

- Conduct a field scale experiment of wind turbine and concentrator to verify if the $k-\varepsilon-f_P$ does not require calibration in their constants when comparing measurements from the inflow transition from undisturbed wind to the rotor's region.

- Explore if there is a correlation between the concentrator speed-up effect, the thrust magnitude force, and the C_T values. If it's confirmed to exist such correlation, then explore the options to adjust these parameters in wind turbine operation to enhance the increment in power production with the presence of a concentrator.

References

Apsley, D., & Castro, I. (1997). A limited-length-scale k-ε model for the neutral and stably-stratified atmospheric boundary layer. *Boundary-Layer Meteorology*, *83*(1), 75–98. https://doi.org/10.1023/A:1000252210512

Atlas, G. W. (2023). *Aerodynamic roughness length and mean wind speed*. Retrieved May 13, 2024, from https://globalwindatlas.info/en

Ávila, M., Gargallo-Peiró, A., & Folch, A. (2017). A CFD framework for offshore and onshore wind farm simulation [Publisher: IOP Publishing]. *Journal of Physics: Conference Series*, *854*, 1–10. https://doi.org/10.1088/1742-6596/854/1/012002

Bechmann, A., Sørensen, N. N., Johansen, J., Vinther, S., Nielsen, B. S., & Botha, P. (2007). Hybrid RANS/LES method for high reynolds numbers, applied to atmospheric flow over complex terrain. *Journal of Physics: Conference Series*, *75*(1), 012054. https://doi.org/10.1088/1742-6596/75/1/012054

Blocken, B., Stathopoulos, T., & Carmeliet, J. (2007). CFD simulation of the atmospheric boundary layer: Wall function problems. *Atmospheric Environment*, *41*(2), 238–252. https://doi.org/https://doi.org/10.1016/j.atmosenv.2006.08.019

Cabezón, D. (2013). *Development of a wake model for wind farms based on an open source CFD solver. strategies on parabolization and turbulence modeling* [Doctoral dissertation, Universidad Politécnica de Madrid]. https://oa.upm.es/21761/1/DANIEL_CABEZON_MARTINEZ.pdf

Cabezón, D., Migoya, E., & Crespo, A. (2011). Comparison of turbulence models for the computational fluid dynamics simulation of wind turbine wakes in the atmospheric boundary layer [_eprint: https://onlinelibrary.wiley.com/doi/pdf/10.1002/we.516]. *Wind Energy*, *14*(7), 909–921. https://doi.org/https://doi.org/10.1002/we.516

Cabezón, D., Sanz, J., Martí, I., & Crespo, A. (2009). CFD modelling of the interaction between the surface boundary layer and rotor wake. comparison of results obtained

with different turbulence models and mesh strategies. *2009*, (n.d.) https://oa.upm.es/21055/1/INVE_MEM_2009_144245.pdf

Calaf, M., Meneveau, C., & Meyers, J. (2010). Large eddy simulations of fully developed wind-turbine array boundary layers. *Physics of Fluids*, *22*(15110), 17. https://doi.org/10.1063/1.3291077

Celik, I., Ghia, U., Roache, P., & Freitas, U. (2008). Procedure for estimation and reporting of uncertainty due to discretization in CFD applications. *Journal of Fluids Engineering*, *130*(78001). https://doi.org/10.1115/1.2960953

Cindori, M., Čajić, P., Džijan, I., Juretić, F., & Kozmar, H. (2022). A comparison of major steady RANS approaches to engineering ABL simulations. *Journal of Wind Engineering and Industrial Aerodynamics*, *221*, 104867. https://doi.org/https://doi.org/10.1016/j.jweia.2021.104867

Cindori, M., Juretić, F., Kozmar, H., & Džijan, I. (2018). Steady RANS model of the homogeneous atmospheric boundary layer. *Journal of Wind Engineering and Industrial Aerodynamics*, *173*, 289–301. https://doi.org/https://doi.org/10.1016/j.jweia.2017.12.006

EIA. (2023). *Wind explained - history of wind power* [Energy explained]. Retrieved May 19, 2024, from https://www.eia.gov/energyexplained/wind/history-of-wind-power.php

Enger, M. (2018). *Wind turbine simulations with OpenFOAM* [Master Thesis]. Norwegian University of Science and Technology. https://ntnuopen.ntnu.no/ntnu-xmlui/bitstream/handle/11250/2496219/18290_FULLTEXT.pdf?sequence=1

Fang, F.-M., & Wang, D. Y. (1997). On the flow around a vertical porous fence. *Journal of Wind Engineering and Industrial Aerodynamics*, *67-68*, 415–424. https://doi.org/10.1016/S0167-6105(97)00090-1

Franke, J., & Baklanov, A. (2007). *Best practice guideline for the CFD simulation of flows in the urban environment: COST action 732 quality assurance and improvement of microscale meteorological models*. European Cooperation in Science; Technology. https://www.researchgate.net/publication/257762102_Best_Practice_Guideline_for_the_CFD_Simulation_of_Flows_in_the_Urban_Environment_COST_Action_732_Quality_Assurance_and_Improvement_of_Microscale_Meteorological_Models

Gargallo-Peiró, A., Ávila, M., Owen, H., Prieto, L., & Folch, A. (2018). Mesh generation, sizing and convergence for onshore and offshore wind farm atmospheric boundary layer ow simulation with actuator discs. *Journal of Computational Physics*, *375*, 209–227. https://doi.org/https://doi.org/10.1016/j.jcp.2018.08.031

Google earth pro. (2023). Retrieved April 15, 2024, from https://www.google.es/maps/@29.2022057,47.0482652,16.17z?hl=es&entry=ttu

Grinderslev, C., Sørensen, N. N., Horcas, S. G., Troldborg, N., & Zahle, F. (2021). Wind turbines in atmospheric flow: Fluid–structure interaction simulations with hybrid turbulence modeling [Publisher: Copernicus GmbH]. *Wind Energy Science*, *6*(3), 627–643. https://doi.org/10.5194/wes-6-627-2021

Hågbo, T., & Giljarhus, K. (2022). Pedestrian wind comfort assessment using computational fluid dynamics simulations with varying number of wind directions. *Frontiers in Built Environment*, *8*, 1–14. https://doi.org/10.3389/fbuil.2022.858067

Hågbo, T., Giljarhus, K., & Hjertager, B. (2021). Influence of geometry acquisition method on pedestrian wind simulations. *Journal of Wind Engineering and Industrial Aerodynamics*, *215*, 104665. https://doi.org/10.1016/j.jweia.2021.104665

Hamlaoui, M. N., Smaili, A., Fellouah, H., & Bouhelal, A. (2023). RANS simulation of two co-axially positioned HAWT under different thermal stratification conditions. *2023 Second International Conference on Energy Transition and Security (ICETS)*, (n.d.) https://doi.org/10.1109/ICETS60996.2023.10410806

Hardy, S. (2017). *Computational fluid dynamics modeling of wind turbine wake using reynolds-averaged navier-stokes and actuator discs* [Master Thesis]. Universitat Autònoma de Barcelona.

Hargreaves, D. M., & Wright, N. G. (2007). On the use of the k–ε model in commercial CFD software to model the neutral atmospheric boundary layer [Number: 5]. *Journal of Wind Engineering and Industrial Aerodynamics*, *95*(5), 355–369. https://doi.org/https://doi.org/10.1016/j.jweia.2006.08.002

Heisler, G. M., & Dewalle, D. R. (1988). 2. effects of windbreak structure on wind flow. *Agriculture, Ecosystems & Environment*, *22-23*, 41–69. https://doi.org/10.1016/0167-8809(88)90007-2

IEC. (2005). Part 1: Design requirements (61400-1:2005e). https://webstore.iec.ch/publication/5426

Javaheri, A., & Cañadillas, B. (2013). Wake modeling of an offshore wind farm using OpenFOAM. *DEWI MAGAZIN*, *43*, 15–21. https://docplayer.net/3117249-Wake-modeling-of-an-offshore-wind-farm-using-openfoam.html

Kasmi, A., & Masson, C. (2008). An extended model for turbulent flow through horizontal-axis wind turbines. *Journal of Wind Engineering and Industrial Aerodynamics*, *96*, 103–122. https://doi.org/10.1016/j.jweia.2007.03.007

KSIR. (n.d.). *Shagaya wind project* [Shagaya wind project]. Retrieved May 13, 2024, from https://www.kisr.edu.kw/en/gi/3/details/

Launder, B. E., & Spalding, D. B. (1974). The numerical computation of turbulent flows. *Computer Methods in Applied Mechanics and Engineering*, *3*(2), 269–289. https://doi.org/10.1016/0045-7825(74)90029-2

Liu, L., & Stevens, R. (2021). Enhanced wind-farm performance using windbreaks. *American Physical Society*, *6*, 1–17. https://doi.org/10.1103/PhysRevFluids.6.07461

Manwell, J. F. (2009). *Wind energy explained: Theory, design and application* (2nd. ed.). John Wiley & Sons.

Marciotto, E. R., & Fisch, G. F. (2013). Investigation of approaching ocean flow and its interaction with land internal boundary layer. *American Journal of Environmental Engineering*, *3*, 18–23. https://api.semanticscholar.org/CorpusID:62823159

Martí, A. (2020). *CFD modeling of atmospheric boundary layer for wind power concentrating systems using commercial CFD solvers* [Master Thesis]. Universitat Rovira i Virgilli.

Monin, A. S., & Obukhov, A. M. (1954). Basic laws of turbulent mixing in the surface layer of the atmosphere. *Tr. Geofiz. Inst. Akad. Nauk. SSSR*, *24*(151), 163–187. https://api.semanticscholar.org/CorpusID:198942767

Navarro, G. (2022). *K-epsilon-fp turbulence model for OpenFOAM 4.1 and OpenFOAM v2012. from van dar laan et al. 2015.* Retrieved February 2, 2024, from https://www.researchgate.net/publication/340929542_code_available_k-epsilon-fp_turbulence_model_for_OpenFOAM_41_and_OpenFOAM_v2012_From_van_dar_Laan_et_al_2015

Navarro, G., Avila, M., & Arnau, F. (2018). An annual energy production estimation methodology for onshore wind farms over complex terrain using a RANS model

with actuator discs. *Journal of Physics*, *1037*, 1–11. https://doi.org/doi:10.1088/1742-6596/1037/7/072018

Ning, L., Yongqian, L., Li, L., & Chang, S. (2021). Numerical simulation of wind turbine wake based on extended k-epsilon turbulence model coupling with actuator disc considering nacelle and tower. *IET Renewable Power Generation*, *14*(18), 3834–3842. https://doi.org/10.1049/iet-rpg.2020.0416

Panofsky, H. A., & Dutton, J. A. (1984). *Atmospheric turbulence : Models and methods for engineering applications / hans a. panofsky, john a. dutton.* [Publication Title: Atmospheric turbulence : models and methods for engineering applications]. Wiley.

Parente, A., Gorlé, C., Van Beeck, J., & Benocci, C. (2011). Improved k–ε model and wall function formulation for the RANS simulation of ABL flows [Number: 4]. *Journal of Wind Engineering and Industrial Aerodynamics*, *99*(4), 267–278. https://doi.org/https://doi.org/10.1016/j.jweia.2010.12.017

Politis, E. S., Prospathopoulos, J., Cabezon, D., Hansen, K. S., Chaviaropoulos, P. K., & Barthelmie, R. J. (2012). Modeling wake effects in large wind farms in complex terrain: The problem, the methods and the issues. *Wind Energy*, *15*(1), 161–182. https://doi.org/10.1002/we.481

Pope, S. B. (2000). *Turbulent flows*. Cambridge University Press.

Ramos, B. (2020). *Proof of concept for concentrated wind power systems* (2020-01/CWPRoof). CEDER-CIEMAT. Laboratorio de Ensayos Eólicos LE.

Ren, H., Zhang, X., Kang, S., & Liang, S. (2019). Actuator disc approach of wind turbine wake simulation considering balance of turbulence kinetic energy. *Energies*, *12*(1), 1–19. https://doi.org/10.3390/en12010016

Réthoré, P., Sørensen, N., Bechmann, A., & Zahle, F. (2009). Study of the atmospheric wake turbulence of a CFD actuator disc model. *EWEC*, 1–9. https://orbit.dtu.dk/en/publications/study-of-the-atmospheric-wake-turbulence-of-a-cfd-actuator-disc-m

Réthoré, P., Van der Laan, P., Troldborg, N., Zahle, N., & Sørensen, N. (2014). Verification and validation of an actuator disc model. *Wind Energy*, *17*, 919–937. https://doi.org/10.1002/we.1607

Ricci, A., Kalkman, I., Blocken, B., Burlando, M., & Repetto, M. P. (2020). Impact of turbulence models and roughness height in 3d steady RANS simulations of wind

flow in an urban environment. *Building and Environment*, *171*, 106617. https://doi.org/https://doi.org/10.1016/j.buildenv.2019.106617

Richards, P. J., & Hoxey, R. P. (1993). Appropriate boundary conditions for computational wind engineering models using the k- turbulence model. *Journal of Wind Engineering and Industrial Aerodynamics*, *46-47*, 145–153. https://doi.org/https://doi.org/10.1016/0167-6105(93)90124-7

Richards, P. J., & Norris, S. E. (2011). Appropriate boundary conditions for computational wind engineering models revisited [Number: 4]. *Journal of Wind Engineering and Industrial Aerodynamics*, *99*(4), 257–266. https://doi.org/https://doi.org/10.1016/j.jweia.2010.12.008

Roache, P. J. (1994). Perspective: A method for uniform reporting of grid refinement studies. *Journal of Fluids Engineering*, *116*(3), 405–413. https://doi.org/10.1115/1.2910291

Schulz, C., Klein, L., Weihing, P., Lutz, T., & Krämer, E. (2014). CFD studies on wind turbines in complex terrain under atmospheric inflow conditions. *Journal of Physics: Conference Series*, *524*(1), 012134. https://doi.org/10.1088/1742-6596/524/1/012134

Simisiroglou, N., Breton, S., & Ivanell, S. (2017). Validation of the actuator disc approach using small-scale model wind turbines. *Wind Energy Science*, *2*, 587–601. https://doi.org/10.5194/wes-2-587-2017

Sørensen, J. N., Nilsson, K., Ivanell, S., Asmuth, H., & Mikkelsen, R. F. (2020). Analytical body forces in numerical actuator disc model of wind turbines. *Renewable Energy*, *147*, 2259–2271. https://doi.org/https://doi.org/10.1016/j.renene.2019.09.134

Tobin, N., & Chamorro, L. (2017). Windbreak effects within infinite wind farms [b]. *Energies*, *10*(1140), 1–12. https://doi.org/10.3390/en10081140

Tobin, N., Hamed, A., & Chamorro, L. (2017). Fractional flow speed-up from porous windbreaks for enhanced wind-turbine power. *Springer Science*, *163*, 253–271. https://doi.org/10.1007/s10546-016-0228-8

van der Laan, P., Baungaard, M., & Kelly, M. (2021). Inflow modeling for wind farm flows in RANS [Publisher: IOP Publishing]. *Journal of Physics: Conference Series*, *1934*(1), 012012. https://doi.org/10.1088/1742-6596/1934/1/012012

van der Laan, P., García-Santiago, O., Sørensen, N., Troldborg, N., Risco, J. C., & Badger, J. (2023). Simulating wake losses of the danish energy island wind farm cluster [c]. *Journal of Physics: Conference Series*, *2505*(1), 1–11. https://doi.org/10.1088/1742-6596/2505/1/012015

van der Laan, P., Murcia, J., Réthoré, P., Mann, J., Kelly, M., Troldborg, N., Hansen, K., & Sørensen, N. (2015). The k-e-fP model applied to wind farms. *Wind Energy*, *18*, 2065–2084. https://doi.org/10.100/we.1804

van der Laan, P., Réthoré, P., Mann, J., Kelly, M., Troldborg, N., Schepers, J., Machefaux, E., & Sørensen, N. (2015). An improved k-ε model applied to a wind turbine wake in atmospheric turbulence. *Wind Energy*, *18*, 889–907. https://doi.org/10.1002/we.1736

van der Laan, P., Sørensen, N., Réthoré, P., Mann, J., Kelly, M., & Troldborg, N. (2014). The k-ε-fP model applied to double wind turbine wakes using different actuator disk force methods. *Wind Energy*, *00*, 2223–2240. https://doi.org/10.1002/we

Venkatraman, K., Hågbo, T.-O., Buckingham, S., & Teigen Giljarhus, K. E. (2023). Effect of different source terms and inflow direction in atmospheric boundary modeling over the complex terrain site of perdigão [Publisher: Copernicus GmbH]. *Wind Energy Science*, *8*(1), 85–108. https://doi.org/10.5194/wes-8-85-2023

WindEurope. (2024). *About wind* [WindEurope asbl/vzw]. Retrieved May 19, 2024, from https://windeurope.org/about-wind/

WTM. (n.d.). *Gamesa g97* [Wind-turbine-models.com]. Retrieved May 13, 2024, from https://en.wind-turbine-models.com/turbines/764-gamesa-g97

W'WAVE. (2022). *Shagaya concentrated wind power project - initial project plan for discussion.*

Yan, B. W., Li, Q. S., He, Y., & Chan, P. (2015). RANS simulation of neutral atmospheric boundary layer flows over complex terrain by proper imposition of boundary conditions and modification on the k-e model [Number: 18 April 2015], *16*(18), 1–23. https://doi.org/10.1007/s10652-015-9408-1

Yang, Y., Gu, M., Chen, S., & Jin, X. (2009). New inflow boundary conditions for modelling the neutral equilibrium atmospheric boundary layer in computational wind engineering [Number: 2]. *Journal of Wind Engineering and Industrial Aerodynamics*, *97*(2), 88–95. https://doi.org/https://doi.org/10.1016/j.jweia.2008.12.001

Zhang, Y., Deng, S., & Wang, X. (2019). RANS and DDES simulations of a horizontal-axis wind turbine under stalled flow condition using OpenFOAM. *Energy*, *167*, 1155–1163. https://doi.org/https://doi.org/10.1016/j.energy.2018.11.014

Zhang, Y. (2018, January 22). *Ground surface effects in wind farms: A micro wind farm model study* [Master Thesis]. Johns Hopkins University. Retrieved May 10, 2024, from http://jhir.library.jhu.edu/handle/1774.2/59219

Appendix A

Appendix

A.1 Met-mast analysis of Shagaya

The following fig. A.1 fig. A.2 are statistics analyzed from a met mast of 78 m of height for wind velocity data series of the period of year 2022.

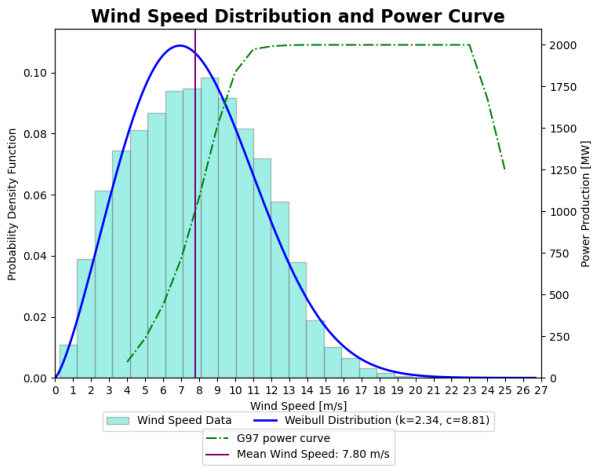

Figure A.1: Weibull distribution of wind speed

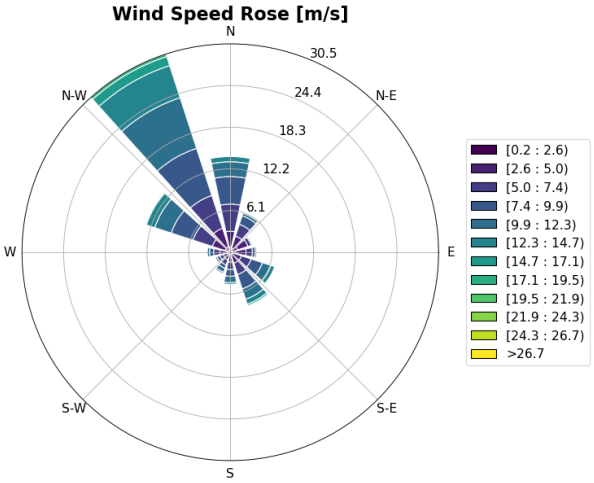

Figure A.2: Wind speed rose

A.2 Hybrid inlet profile U for CIEMAT

The following is the inlet boundary condition used for hybrid inlet profile with 02 values of z_o used in section 2.4.2:

```
inlet
{
```

```
type            codedFixedValue;
value           $internalField;
name  myInletProfile;
code
#{
const vectorField& Cf = patch().Cf();
vectorField& field = *this;
const scalar kappa = 0.40;
forAll(Cf, faceI)
{
    const scalar z = Cf[faceI][2];
    if (z <= 10.24)
    {
        const scalar uStar = 0.3078;
        const scalar z0 = 0.0025;
        field[faceI] = vector((uStar/kappa)*log((z+z0)/z0),0,0);
    }
    else
    {
        field[faceI] = vector((1/0.6312)*log(z/0.1803),0,0);
    }
}
#};
}
```

A.3 vectorCodedSource NREL thrust distribution

The present snippet code is the implementation via vectorCodedSource tool to implement custom source term in the momentum equation. Here is use a prescribed force magnitude with a radial load distribution of the case used in section 2.5.5 and in calibration process of table 3.6.

```
myradialAD
```

```
{
type            vectorCodedSource;
selectionMode   cellSet;
cellSet        actuationDisk1CellSet;
fields          (U);
name            myradialAD;
codeCorrect
#{ #};
codeConstrain
#{ #};
codeAddSup
#{
vectorField& Usource = eqn.source();
const Field<vector> zoneCellCentres(mesh().cellCentres(), cells_);
const Field<scalar> zoneCellVolumes(mesh().cellVolumes(), cells_);
const vector avgCentre = gSum(zoneCellVolumes*zoneCellCentres)/V();
const scalar maxR = gMax(mag(zoneCellCentres - avgCentre));
const scalarField& V = mesh_.V();
const scalar Uref = 8;
const scalar diskArea = 12469;
const scalar T = 0.5*diskArea*pow(Uref,2)*Ct;
vector dir(1,0,0);
vector sourcesAD(Zero);
const labelList& cellIDs = cells();
scalar magUsource = 0.0;
forAll(cellIDs, i)
{
label cellI = cellIDs[i];
const scalar rPos = mag(mesh().cellCentres()[cellI] - avgCentre);

//Calc of distribution for thrust - ORIGINAL NREL distribution
const scalar rRatio3 = -(27.0/4.0) * (pow(rPos,2.0)*(rPos-maxR))/
```

```
   (pow(maxR,3.0));
const scalar rRatio9 = -(387420489.0/16777216.0)*(pow(rPos,8.0) /
  (rPos-maxR))/(pow(maxR,9.0));
const scalar rRatio = 1.54*1.19*(0.5*rRatio3 + 0.5*rRatio9);
sourcesAD.x() = (T) * rRatio * (V[cellI]/V_);
sourcesAD.y() = 0;
sourcesAD.z() = 0;
Usource[cellI] += sourcesAD;
magUsource += sourcesAD.x();
}
reduce(magUsource, sumOp<scalar>());
Info << " The thrust is T = " << T << endl;
Info << " The total amount of sink term applied
         is magUsource = " << magUsource << endl;

#};
}
```

A.4 vectorCodedSource Variable thrust force controller

Here is introduce the snippet code of vectorCodedSource for the controler method. The reading table is introduce as separate list of scalars and a check of values is executed in every iteration.

```
ADM2
{
type            vectorCodedSource;
selectionMode   cellSet;
cellSet        actuationDisk2CellSet;
fields          (U);
name            calibratedADM2;
codeCorrect
#{ #};
```

```
codeConstrain
#{ #};
codeAddSup
#{
vectorField& Usource = eqn.source();
const vectorField& U = eqn.psi();
const scalarField& cellsV = mesh_.V();
vector diskDir_(1,0,0);
const scalar diskArea =  12468;
List<scalar> UadList_(20);
UadList_[0] = 1.631 ;
UadList_[1] = 2.249 ;
UadList_[2] = 3.183 ;
UadList_[3] = 3.783 ;
UadList_[4] = 4.326 ;
UadList_[5] = -1.000 ;
UadList_[6] = -1.000 ;
UadList_[7] = -1.000 ;
UadList_[8] = -1.000 ;
UadList_[9] = -1.000 ;
UadList_[10] = -1.000 ;
UadList_[11] = -1.000 ;
UadList_[12] = -1.000 ;
UadList_[13] = -1.000 ;
UadList_[14] = -1.000 ;
UadList_[15] = -1.000 ;
UadList_[16] = -1.000 ;
UadList_[17] = -1.000 ;
UadList_[18] = -1.000 ;
UadList_[19] = -1.000 ;
List<scalar> UrefList_(20);
UrefList_[0] = 4.000 ;
```

```
UrefList_[1] = 5.000 ;
UrefList_[2] = 6.000 ;
UrefList_[3] = 7.000 ;
UrefList_[4] = 8.000 ;
UrefList_[5] = -1.000 ;
UrefList_[6] = -1.000 ;
UrefList_[7] = -1.000 ;
UrefList_[8] = -1.000 ;
UrefList_[9] = -1.000 ;
UrefList_[10] = -1.000 ;
UrefList_[11] = -1.000 ;
UrefList_[12] = -1.000 ;
UrefList_[13] = -1.000 ;
UrefList_[14] = -1.000 ;
UrefList_[15] = -1.000 ;
UrefList_[16] = -1.000 ;
UrefList_[17] = -1.000 ;
UrefList_[18] = -1.000 ;
UrefList_[19] = -1.000 ;
// Initialize CtList_
List<scalar> CtList_(20);
CtList_[0] = 0.900 ;
CtList_[1] = 0.860 ;
CtList_[2] = 0.780 ;
CtList_[3] = 0.770 ;
CtList_[4] = 0.770 ;
CtList_[5] = -1.000 ;
CtList_[6] = -1.000 ;
CtList_[7] = -1.000 ;
CtList_[8] = -1.000 ;
CtList_[9] = -1.000 ;
CtList_[10] = -1.000 ;
```

```
CtList_[11] = -1.000 ;
CtList_[12] = -1.000 ;
CtList_[13] = -1.000 ;
CtList_[14] = -1.000 ;
CtList_[15] = -1.000 ;
CtList_[16] = -1.000 ;
CtList_[17] = -1.000 ;
CtList_[18] = -1.000 ;
CtList_[19] = -1.000 ;
vector Udisk(Zero);
scalar totalV = 0.0;
for (const label celli : cells_)
{
Udisk += U[celli]*cellsV[celli];
totalV += cellsV[celli];
}
reduce(Udisk, sumOp<vector>());
reduce(totalV, sumOp<scalar>());
Udisk /= totalV;
// variable READ of disk-average x-component (streamwise) of
wind speed for lookup inside lists
scalar Uadx = Udisk.x();
// variable that will store undisturbed WS for thrust magnitude
computation based on calibration test
scalar UrefNew = 0.0;
// variable that will store thrust coeff for thrust magnitude
computation based on calibration test
scalar CtrefNew = 0.0;
label count = 20;
label zeroPos = UadList_.find(-1); // function find() will return
index -1 in case does not find the flag
if(zeroPos != -1)
```

```
{
count = zeroPos;
}
// in case Uadx is lower than the fist value from calibration
procedure list:
if(Uadx < UadList_[0])
{
UrefNew = UrefList_[0] - (UrefList_[1] - UrefList_[0])*((UadList_[0]- Uadx)/
(UadList_[1]-UadList_[0]));
CtrefNew = (CtList_[0] - (CtList_[1] - CtList_[0])*((UadList_[0]-Uadx)/
(UadList_[1]-UadList_[0])));
}
// in case Uadx is higher than the last(maximum) value from
calibration procedure list:
else if(Uadx > UadList_[count-1])
{
UrefNew = UrefList_[count-1] + (UrefList_[count-1] - UrefList_[count-2])*
((Uadx - UadList_[count-1])/
(UadList_[count-1]-UadList_[count-2]));
CtrefNew = (CtList_[count-1] + (CtList_[count-1] - CtList_[count-2])*
((Uadx - UadList_[count-1])/
(UadList_[count-1]-UadList_[count-2])));
}
// in case Uadx is between UadList_[0] and UadList_[count-1],
then:
else
{
for(int i=1; i < count; i++)
{
if(Uadx > UadList_[i])
{
continue;
```

```
}
else
{
UrefNew = UrefList_[i-1] - (UrefList_[i] - UrefList_[i-1]) *
( (UadList_[i-1] - Uadx)  /( UadList_[i] - UadList_[i-1] ) );
CtrefNew = (CtList_[i-1] - (CtList_[i] - CtList_[i-1]) *
( (UadList_[i-1] - Uadx) / (UadList_[i] - UadList_[i-1] ) ));
break;
}
}
}
const scalar T = 0.5*diskArea*pow(UrefNew,2)*CtrefNew;
scalar magSource = 0.0;
const Field<vector> zoneCellCentres(mesh().cellCentres(), cells_);
const Field<scalar> zoneCellVolumes(mesh().cellVolumes(), cells_);
const vector avgCentre = gSum(zoneCellVolumes*zoneCellCentres)/V();
const scalar maxR = gMax(mag(zoneCellCentres - avgCentre));
for (const label celli : cells_)
{
const scalar rPos = mag(mesh().cellCentres()[celli] - avgCentre);
//Calc of distribution for thrust - ORIGINAL NREL distribution
const scalar rRatio3 = -(27.0/4.0) * (pow(rPos,2.0)*(rPos-maxR))/
(pow(maxR,3.0));
const scalar rRatio9 = -(387420489.0/16777216.0)*
(pow(rPos,8.0)*(rPos-maxR))/(pow(maxR,9.0));
const scalar rRatio = 1.54*1.19*(0.5*rRatio3 + 0.5*rRatio9);
Usource[celli] += ((cellsV[celli]/totalV)*T*rRatio)*diskDir_;
magSource += mag(Usource[celli]&diskDir_);
}
reduce(magSource, sumOp<scalar>());
Info << " The Uadx is = " << Uadx << " in " << this->name() << endl;
Info << " The UrefNew is = " << UrefNew << " in " << this->name()<< endl;
```

```
Info << " The CtrefNew is = " << CtrefNew << " in " <<
this>name()<< endl;
Info << " The thrust is T = " << T << " in " << this->name() << endl;
Info << " The total amount of sink term applied is magUsource = "
<< magSource << " in " << this->name() << endl;
#};
}
```